Computational modeling of coronary tortuosity

Natalya Vorobtsova

Thesis submitted to the faculty of the Virginia Polytechnic Institute and State University in partial fulfillment of the requirements for the degree of

Master of Science
In
Mechanical Engineering

Pavlos Vlachos, Co-Chair
Mark Stremler, Co-Chair
David Sane

1.27.2015
Blacksburg, Virginia

Keywords: coronary arteries, tortuosity, hemodynamics, wall shear stress, pressure drop, artherosclerosis, ischemia

Computational modeling of coronary tortuosity

Natalya Vorobtsova

Abstract

Coronary tortuosity is the abnormal curving and twisting of the coronary arteries. Although the phenomenon of coronary tortuosity is frequently encountered by cardiologists its clinical significance is unclear. It is known that coronary tortuosity has significant influence on the hemodynamics inside the coronary arteries, but it is difficult to draw definite conclusions due to the lack of patient-specific studies and an absence of a clear definition of tortuosity.

In this work, in order to investigate a relation of coronary tortuosity to such diseases as atherosclerosis, ischemia, and angina, a numerical investigation of coronary tortuosity was performed. First, we studied a correlation between a degree of tortuosity and flow parameters in three simplified vessels with curvature and zero torsion. Next, a statistical analysis based on flow calculations of 23 patient-based real tortuous arteries was performed in order to investigate a correlation between tortuosity and flow parameters, such as pressure drop, wall shear stress distribution, and a strength of helical flow, represented by a helicity intensity, and concomitant risks.

Results of both idealized and patient-specific studies indicate that a risk of perfusion defects grows with an increased degree of tortuosity due to an increased pressure drop downstream an artery. According to the results of the patient-specific study, a risk of atherosclerosis decreases in more tortuous arteries – a result different from an outcome of the idealized study of arteries with zero torsion. Consequently, a modeling of coronary tortuosity should take into account all aspects of tortuosity including a heart shape that introduces additional torsion to arteries. Moreover, strength of a helical flow was shown to depend strongly on a degree of tortuosity and affect flow alterations and accompanying risks of developing atherosclerosis and perfusion defects. A corresponding quantity, helicity intensity, might have a potential to be implemented in future studies as a universal single parameter to describe tortuosity and assess congruent impact on the health of a patient.

Acknowledgements

I would like to thank my advisors, Dr. Vlachos and Dr. Stremler, for their guidance and mentoring during all the time I spent at VT. I would like to particularly thank Dr. Vlachos for hiring me and giving an opportunity to continue my studies in VT to acquire extremely valuable experience working at the AEThER laboratory.

An existence of this thesis owes a great deal to help of Dr. Miglivacca and Dr. Claudio Chiastra. I would like to thank them for their valuable contribution, sharing their experience, spending time helping to solve the issues with computational modeling, and for their very prompt responses and professional attitude.

The work would not be done without clinical data provided by Dr. Sane and his research group at Carilion Clinic Cardiology. I would also like to thank Dr. Sane for a valuable insight into the clinical aspects of the work.

I would like to thank past and current AEThER laboratory members for their help, advice, productive lab meeting discussions, and a good time spent together in the lab.

Finally, I would like to express my gratitude for the support of my friends and family, and especially my husband, Alexandr, my best friend and greatest supporter, for his caring, his love, and patience.

Attribution

The main chapter of this thesis represents an original manuscript under review.

Dr. Pavlos P. Vlachos, Ph.D., Professor of Mechanical Engineering and Biomedical Engineering, Purdue University, is a committee co-chair and has provided advice and insight for the work described in each chapter. Dr. Vlachos is a co-author on the manuscript in Chapter 2.

Dr. Mark A. Stremler, Ph.D., Associate Professor and Director of Research and Graduate Studies for the Department of Engineering Science and Mechanics, Virginia Polytechnic Institute and State University, is a committee co-chair and has provided advice and insight for the work described in each chapter. Dr. Stremler is a co-author on the manuscript in Chapter 2.

Dr. David C. Sane, MD, Chief of Section of Cardiology, Carilion Cardiology Clinic, is a committee member and has provided advice and insight for the work described in each chapter. Dr. Sane also helped acquire the clinical data for the geometry construction for patient-specific studies.

Dr. Francesco Migliavacca, Ph.D., Associate Professor of Department of Chemestry, Materials and Chemistry Engineering 'Giulio Natta', Laboratory of Biological Structure Mechanics, Department of Chemestry, Politecnico di Milano, has provided advice and insight for the work described in each chapter. Dr. Migliavacca is a co-author on the manuscript in Chapter 2.

Dr. Claudio Chiastra, Ph.D., Scientist at Laboratory of Biological Structure Mechanics, Department of Chemestry, Materials and Chemistry Engineering 'Giulio Natta', Politecnico di Milano, has provided advice and insight for the work described in each chapter. Dr. Chiastra is a co-author on the manuscript in Chapter 2.

Table of Contents

List of Figures

List of Tables

List of Abbreviations

3-D	Three-dimensional
ATR	Atrial branch
CAD	Computer-aided design
CTA	Computed tomography angiography
DM	Distance metric
LAD	Left anterior descending artery
LCX	Left circumflex artery
LMCA	Left main coronary artery
LNH	Local normalized helicity
MARG	Marginal branch
RDE	Relative discretization error
RRT	Relative residence time
SPT	Septal artery
TAWSS	Time-averaged wall shear stress
TC	Total curvature
TI	Tortuosity index
TT	Total torsion
WSS	Wall shear stress

1 Introduction

1.1 Motivation

Coronary arteries are relatively straight blood vessels running on the surface of the pericardium that supply the heart muscle with blood. Tortuous coronary vessels take abnormally curved or helically coiled paths, which may have turns and loops (1-5). These abnormal geometries may lead to flow alterations that can cause reduced blood supply to the heart tissues and lead to ischemia (2). An example of straight and tortuous coronary arteries is shown in Figure 1.

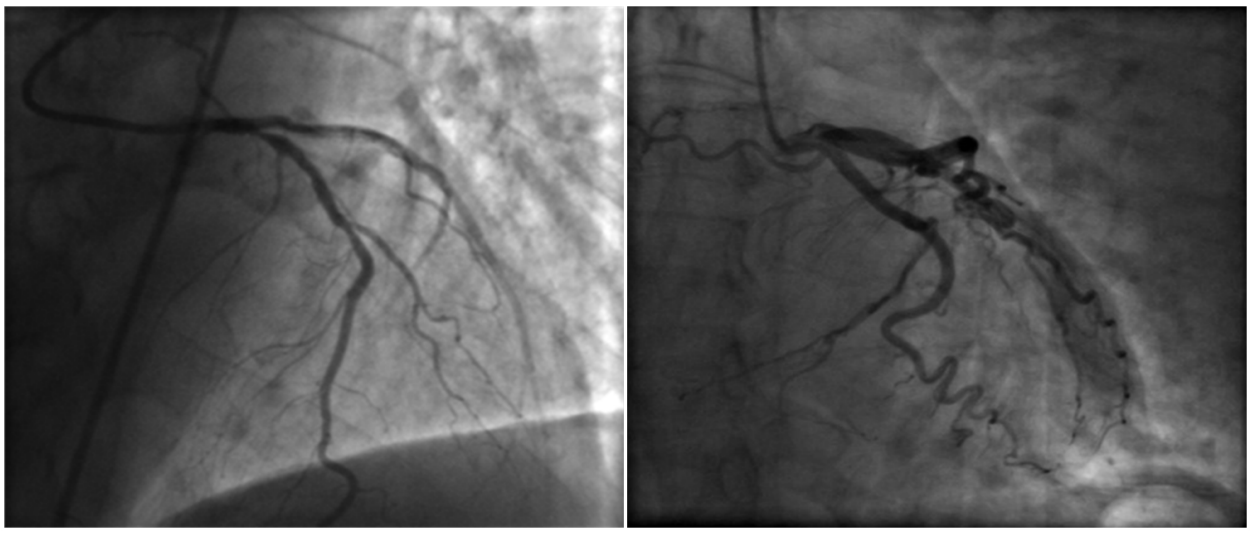

Figure 1. Coronary angiogram showing normal coronary arteries (a) and tortuous coronary arteries (b).

Although cardiologists often encounter coronary tortuosity, its mechanisms and impacts are not well studied. It is well-known that coronary tortuosity is often correlated with such clinical conditions as coronary artery disease (1), diabetes (6), myocardial infarction (3), hypertension (7), and age (2-4, 7, 8). However, even when no other diseases or abnormalities are present, tortuosity can cause various dysfunctions. For patients with normal or near-normal coronary angiograms the prevalence of severely tortuous coronary arteries was reported to be seven times higher in patients who demonstrated reversible perfusion defects compared to those without it (9). Tortuosity is also believed to influence the risk of developing atherosclerosis (2, 10). Understanding coronary tortuosity could help explain chest pain or positive stress tests in the absence of significant luminal stenosis in the epicardial coronary arteries (9), as well as its relation to atherosclerosis.

1.2 Background

1.2.1 Initiation and development

Tortuosity is widely observed in vessels of different ranges: from large arteries and veins, such as the carotid and femoral arteries, to small arterioles and venules, like retinal arteries (1). Clinical and experimental evidence show that tortuosity can be developed due to mechanical factors, such as transmural pressure (11), blood pressure (12, 13), blood flow(14), axial tension (15), and wall structural changes (1, 12). Another possible reason for the initiation of tortuosity is that helical shape provides relaminarization of the flow, as shown experimentally (16). It was also observed that a curved pipe has a higher critical Reynolds number, from which turbulence can occur, than a straight one (17). Even though a coronary flow is not turbulent in general, curvature in large vessels can cause instabilities on the outer bend of the vessel wall (18).

1.2.2 Tortuosity characterization, Tortuosity metrics

Vascular tortuosity has been rated by the degree of tortuosity using an arbitrary scale: mild, moderate, severe, and extreme (13, 19, 20). While mild tortuosity of coronaries is often asymptomatic, severe tortuosity may lead to angina during exercise, a positive stress test, or a myocardial ischemic attack (1, 9, 21). However, that correlation is subjective since no acceptable definition of severe or mild tortuosity exists to date, and there is no “gold-standard” available to measure tortuosity.

A widely used approach to geometrically define the vessel is by characterization of its centerline (22-25). Tortuosity of the centerline of a coronary artery can be considered as an interplay between lengthening, curvature, and torsion. For coronary arteries, or vessels lying on the surface of the heart, the distance between its end points can be assumed fixed. Thus, the lengthening of the vessel causes an increase in curvature and torsion, as well as increasing curvature and torsion effect lengthening of the vessel. Consequently, measurements of curvature and torsion will contain information on the lengthening of the vessel and vice versa.

Tortuosity can be qualitatively characterized with various tortuosity metrics such as: distance metric or relative length variation metric (1, 6, 10, 24, 26-28), inflection count metric (6), sum of angles metric (6), total torsion (29) and total curvature (28, 29) metrics, average torsion (26) and

average curvature (26) metric, total squared curvature (28), normalized root-mean squared curvature (13), etc. All of these metrics represent different aspects of tortuosity. Some of them were found appropriate for specific types of tortuosity, for example, the sum of angles metric was shown to be good for measuring tortuosity of tight low-amplitude coils (6), while the distance metric and inflection count metric are good for broad meandering curves (6).

1.2.3 Computational modeling

To make the simulations more realistic, computational models have to include many complex properties of the flow in an actual tortuous vessel, such as non-Newtonian behavior of the blood and influence of the downstream vasculature on the flow in the computational domain. Although the Newtonian model was shown adequate for describing relevant mean physical parameters under pulsatile flow with moderate Reynolds number flow conditions in coronary arteries, implementing a non-Newtonian character of blood flow gets more and more important for such flow parameters as wall shear in the region of curvatures due to shear induced dilution (30-33). The curvature-induced secondary flow was found to be less dominant for the non-Newtonian fluid than for Newtonian model (33) which is often used to model the blood in tortuous arteries (27, 34-38).

The solution of the blood flow in coronary arteries is highly dependent on the outflow boundary conditions. For the studies where the pressure field distribution is not investigated and only the pressure gradients are calculated, the simplest way to set up boundary conditions for transient coronary flow calculations with one outlet is to prescribe a realistic velocity profile at the inlet and constant pressure at the outlet. The constant boundary condition was shown to give unrealistic results for multiple outlets models (39, 40), and, for the cases with several outlets, the radius-dependent flow split boundary condition can be applied (40, 41).

As numerical models get more advanced, more realistic boundary conditions are introduced to consider the influence of the downstream or upstream vasculatures on the computational domain. Using simple models, the downstream vasculatures can be taken into account by such boundary conditions as the resistance model, Windkessel model, or other lumped parameter models which couple flow rate and pressure in the numerical domain to a reduced-order model or “lumped

parameter" model (39, 40, 42, 43). A general difficulty for setting up these types of boundary conditions is to define the parameters required for each outlet to set them up.

1.2.3.1 Flow in tortuous arteries

To properly understand why the coronary tortuosity may introduce dysfunctions to an otherwise healthy system, its fluid dynamics has to be explored and described in details. The theoretical, experimental, and numerical studies have been carried out to investigate the laminar flow in three-dimensional idealized models such as flow in the bends of constant curvature (44-47), helically coiled pipes of constant curvature and torsion (38, 45), idealized helical arterio-venous graft designs (48), S shaped pipes with planar centerline (36, 37, 49) and with torsion (36, 50), and two subsequent S-shaped vessels (36).

Development of the image-based vessel modeling technologies allowed for the better insight on the processes happening inside real arteries. Flow in the patient-based tortuous coronary arteries (34, 35, 37), tortuous femoral artery (27), and non-planar carotid bifurcations (26) has been previously investigated.

1.2.3.1.1 Secondary motions

The curvature-dependent forces and torsional forces were found to drive secondary motions of the flow (36). Curvature generates motions in the normal to the axial direction (51), firstly investigated by Dean (44), creating helical motions of the flow. In some specific cases the set of parameters describing the curvature dependent secondary motions can be reduced to only one parameter, an example of such is the Dean flow (44, 52). Thus, the helical flow in common carotid arteries is primarily driven by curvature (26). Torsional forces break the symmetry of the helical structures generated by curvature-dependent forces making one structure more dominant (36).

1.2.3.1.2 WSS

Atherosclerotic lesions are believed to appear in the regions of low or oscillatory wall shear stress (WSS), or, as we will denote it further, the regions of "disturbed" WSS (53). This may be explained by an increased uptake of the blood-borne particles in the area of low WSS to the wall

prevalent in atherosclerosis (54) and to the fact that oscillatory and low WSS lead to the longer stay of the particle near the wall (55).

Numerical investigation of the helical motion in the curved pipe without torsion was found to lead to a larger region of disturbed WSS (37). Torsion leads to a more complex flow field that reduces the area zones exposed to atherogenous conditions (48). Moreover, torsion was shown to lead to a more uniform spatial distribution of the WSS (51), which according to Caro *et al.* (56) reduces the risk of vessel occlusion.

While in an idealized study it is easy to consider different aspects of tortuosity separately, the patient-based studies have some specific configurations of those aspects. For example, the coronary arteries will always have some tortuosity due to the inherent shape of the heart. Patient-specific numerical simulations have shown that the lumen shear stress was altered significantly in the presence of vessel tortuosity (27, 35, 37, 57).

As the coronary tortuosity and tortuosity in general is not well defined in the literature and not well understood, it is difficult to draw definite conclusions about the influence of tortuosity on susceptibility of arteries to atherosclerosis, especially considering a very limited number of patient-specific studies. A statistical approach and a consideration of different aspects of tortuosity is really necessary to define coronary tortuosity and to understand the relation between tortuosity and WSS distribution. An example of how the statistical approach can be applied to investigate tortuosity can be seen in the Gallo *et al.* study (26, 57). In these studies, the authors have shown that high values of curvature-driven helicity in the carotid bifurcation is instrumental in suppressing the disturbances in the wall shear stress distribution based on the investigation of 50 patient-specific carotid bifurcations. They also showed that this effect can be moderated when one helical structure is dominant in the flow (57).

1.2.3.1.3 Pressure Drop

An influence of the tortuosity on the pressure drop or driving pressure in a tortuous artery was also investigated in several works. For example, it was shown numerically that, for a steady blood flow through the coiled structure of an umbilical artery, the driving pressure for a given blood flow rate goes up as the number of coils in the cord structure increases (38). The driving pressure gradient also varies with the coils' spreading or pitch: increasing the pitch decreases the

driving pressure gradient (38). The pressure drop in the curved pipe without torsion was also found to be larger than the pressure drop for the same flow rate in the corresponding straight pipe of the same length (45). Patient-specific numerical simulations of Xie *et al*. (34) have shown that the resistance to the blood flow increases in the presence of tortuosity. However, there is a lack of patient-specific work investigating the influence of the coronary tortuosity on the decrease of pressure downstream.

1.3 Our Work

The objective of the current work is to investigate how the coronary flow parameters (pressure drop and hemodynamic descriptors) are affected by different aspects of tortuosity such as curvature, torsion, and lengthening due to tortuosity. We chose the total curvature, total torsion, and distance metrics respectively to quantify them. We aim to investigate a relation between the degree of tortuosity, as measured by these metrics, and flow hemodynamics by means of computation fluid dynamics (CFD) modeling. To fulfill this goal, we performed calculations of three-dimensional idealized and patient-based geometries. In the idealized study, we focus on the influence of curvature without torsion on the flow in the vessel. The patient-specific analysis is based on three patient-specific cases having tortuous left coronary artery trees. The patient-based models were built using segmentation of the vessels from the 3-D coronary CT angiograms. The total number of patient-specific cases considered in the study is three and, considering each branch of the patient vessel separately, resulted in 23 vessel segments. A statistical analysis was performed to explore a dependence of the flow parameters on the multi-aspect nature of tortuosity and an importance of accounting for the inherent curvature of the heart when modeling tortuosity.

1.4 Structure of thesis

The thesis is organized as follows: Chapters 1 provides introduction and the in-depth literature review of the research previously done on the vessel tortuosity. The Chapter 2 represents the original work, presented as a complete manuscript formatted for journal publication. Chapter 3 provides a conclusion and suggestions for the future steps. Appendices provide additional details on the modeling which were not included in the Chapter 2.

References

1. Han HC. Twisted Blood Vessels: Symptoms, Etiology and Biomechanical Mechanisms. Journal of Vascular Research. 2012;49(3):185-97.

2. Zegers ES, Meursing BTJ, Zegers EB, Ophuis AJMO. Coronary tortuosity: a long and winding road. Netherlands Heart Journal. 2007;15(5):191-5.

3. Hutchins GM, Miner MM, Bulkley BH. Tortuosity as an index of the age and diameter increase of coronary collateral vessels in patients after acute myocardial infarction. The American Journal of Cardiology. 1978;41(2):210-5.

4. Turgut O, Yilmaz A, Yalta K, Yilmaz B, Ozyol A, Kendirlioglu O, et al. Tortuosity of coronary arteries: an indicator for impaired left ventricular relaxation? The International Journal of Cardiovascular Imaging. 2007;23(6):671-7.

5. Barilla F, Romeo F, Rosano GMC, Valente A, Reale A. Coronary artery loops and myocardial ischemia. American Heart Journal. 1991;122(1):225-6.

6. Bullitt E, Gerig G, Pizer SM, Lin W, Aylward SR. Measuring tortuosity of the intracerebral vasculature from MRA images. IEEE transactions on medical imaging. 2003;22(9):1163-71.

7. Del Corso L, Moruzzo D, Conte B, Agelli M, Romanelli AM, Pastine F, et al. Tortuosity, kinking, and coiling of the carotid artery: expression of atherosclerosis or aging? Angiology. 1998;49(5):361-71.

8. Soikkonen K, Wolf J, Mattila K. Tortuosity of the lingual artery and coronary atherosclerosis. British Journal of Oral & Maxillofacial Surgery. 1995;33(5):309-11.

9. Gaibazzi N, Rigo F, Reverberi C. Severe Coronary Tortuosity or Myocardial Bridging in Patients With Chest Pain, Normal Coronary Arteries, and Reversible Myocardial Perfusion Defects. The American Journal of Cardiology. 2011;108(7):973-8.

10. Smedby Ö, Bergstrand L. Tortuosity and atherosclerosis in the femoral artery: What is cause and what is effect? Annals of Biomedical Engineering. 1996;24(4):474-80.

11. Kylstra JA, Wierzbicki T, Wolbarsht ML, Landers rMB, Stefansson E. The relationship between retinal vessel tortuosity, diameter, and transmural pressure. Graefe's archive for clinical and experimental ophthalmology = Albrecht von Graefes Archiv für klinische und experimentelle Ophthalmologie. 1986;224(5):477-80.

12. Cheung CY-L, Zheng Y, Hsu W, Lee ML, Lau QP, Mitchell P, et al. Retinal vascular tortuosity, blood pressure, and cardiovascular risk factors. Ophthalmology. 2011;118(5):812-8.

13. Dougherty G, Johnson MJ, Wiers MD. Measurement of retinal vascular tortuosity and its application to retinal pathologies. Medical & Biological Engineering & Computing. 2010;48(1):87-95.

14. Sutter FKP, Helbig H. Familial retinal arteriolar tortuosity: A review. Survey of Ophthalmology. 2003;48(3):245-55.

15. Jackson ZS, Dajnowiec D, Gotlieb AI, Langille BL. Partial off-loading of longitudinal tension induces arterial tortuosity. Arteriosclerosis, thrombosis, and vascular biology. 2005;25(5):957-62.

16. Narasimha R, Sreenivasan KR. Relaminarization of Fluid Flows. 19: Elsevier Science & Technology; 1979. p. 221-309.

17. Srivastava RS. Turbulence: pipe flows. New Delhi: Indian National Science Academy; 1977.

18. Papageorgiou D. Stability of the unsteady viscous flow in a curved pipe. Journal of Fluid Mechanics. 1987;182:209-33.

19. Johnson MJ, Dougherty G. Robust measures of three-dimensional vascular tortuosity based on the minimum curvature of approximating polynomial spline fits to the vessel mid-line. Med Eng Phys. 2007;29(6):677-90.

20. Wolf YG, Tillich M, Lee WA, Rubin GD, Fogarty TJ, Zarins CK. Impact of aortoiliac tortuosity on endovascular repair of abdominal aortic aneurysms: Evaluation of 3D computer-based assessment. Journal of Vascular Surgery. 2001;34(4):594-9.

21. Gaibazzi N. Less than "straight" anginal symptoms. International journal of cardiology. 2011;148(3):385-6.

22. Choi G, Cheng CP, Wilson NM, Taylor CA. Methods for quantifying three-dimensional deformation of arteries due to pulsatile and nonpulsatile forces: implications for the design of stents and stent grafts. Ann Biomed Eng. 2009;37(1):14-33.

23. Dougherty G, Johnson MJ. Clinical validation of three-dimensional tortuosity metrics based on the minimum curvature of approximating polynomial splines. Medical Engineering and Physics. 2008;30(2):190-8.

24. Piccinelli M, Veneziani A, Steinman DA, Remuzzi A, Antiga L. A Framework for Geometric Analysis of Vascular Structures: Application to Cerebral Aneurysms. IEEE Transactions on Medical Imaging. 2009;28; 31(8):1141-55.

25. Sangalli LM, Secchi P, Vantini S, Veneziani A. A Case Study in Exploratory Functional Data Analysis: Geometrical Features of the Internal Carotid Artery. Journal of the American Statistical Association. 2009;104(485):37-48.

26. Gallo D, Steinman DA, Morbiducci U. An Insight into the Mechanistic Role of the Common Carotid Artery on the Hemodynamics at the Carotid Bifurcation. Ann Biomed Eng. 2014.

27. Wood NB, Zhao SZ, Zambanini A, Jackson M, Gedroyc W, Thom SA, et al. Curvature and tortuosity of the superficial femoral artery: a possible risk factor for peripheral arterial disease. J Appl Physiol. 2006;101(5):1412-8.

28. Hart WE, Goldbaum M, Côté B, Kube P, Nelson MR. Measurement and classification of retinal vascular tortuosity. International journal of medical informatics. 1999;53(2-3):239-52.

29. O'Flynn PM, O'Sullivan G, Pandit AS. Methods for three-dimensional geometric characterization of the arterial vasculature. Annals of Biomedical Engineering. 2007;35(8):1368-81.

30. Van Wyk S, Prahl Wittberg L, Fuchs L. Wall shear stress variations and unsteadiness of pulsatile blood-like flows in 90-degree bifurcations. Computers in biology and medicine. 2013;43(8):1025-36.

31. Ku DN. Blood Flow in Arteries. Annual Review of Fluid Mechanics. 1997;29(1):399-434.

32. Samady H, Eshtehardi P, McDaniel MC, Suo J, Dhawan SS, Maynard C, et al. Coronary artery wall shear stress is associated with progression and transformation of atherosclerotic plaque and arterial remodeling in patients with coronary artery disease. Circulation. 2011;124(7):779-88.

33. Chen J, Lu XY. Numerical investigation of the non-Newtonian pulsatile blood flow in a bifurcation model with a non-planar branch. Journal of Biomechanics. 2006;39(5):818-32.

34. Xie X, Wang Y, Zhu H, Zhou H, Zhou J. Impact of Coronary Tortuosity on Coronary Blood Supply: A Patient-Specific Study. PLoS ONE. 2013;8(5):e64564.

35. Prosi M, Perktold K, Ding Z, Friedman MH. Influence of curvature dynamics on pulsatile coronary artery flow in a realistic bifurcation model. Journal of Biomechanics. 2004;37(11):1767-75.

36. Alastruey J, Siggers JH, Peiffer V, Doorly DJ, Sherwin SJ. Reducing the data: Analysis of the role of vascular geometry on blood flow patterns in curved vessels. Physics of Fluids. 2012;24(3):031902.

37. Xie X, Wang Y, Zhu H, Zhou J. Computation of hemodynamics in tortuous left coronary artery: a morphological parametric study. Journal of Biomechanical Engineering. 2014;136(10):101006.

38. Kaplan AD, Jaffa AJ, Timor IE, Elad D. Hemodynamic Analysis of Arterial Blood Flow in the Coiled Umbilical Cord. Reproductive Sciences. 2010;17(3):258-68.

39. Vignon-Clementel IE, Alberto Figueroa C, Jansen KE, Taylor CA. Outflow boundary conditions for three-dimensional finite element modeling of blood flow and pressure in arteries. Computer Methods in Applied Mechanics and Engineering. 2006;195(29–32):3776-96.

40. Sommer K, Schmidt R, Graafen D, Breit HC, Schreiber LM. Contrast agent bolus dispersion in a realistic coronary artery geometry: influence of outlet boundary conditions. Ann Biomed Eng. 2014;42(4):787-96.

41. Chiastra C, Morlacchi S, Gallo D, Morbiducci U, Cárdenes R, Larrabide I, et al. Computational fluid dynamic simulations of image-based stented coronary bifurcation models. Journal of the Royal Society, Interface / the Royal Society. 2013;10(84):20130193.

42. Williams AR, Koo B-K, Gundert TJ, Fitzgerald PJ, LaDisa JJF. Local hemodynamic changes caused by main branch stent implantation and subsequent virtual side branch balloon angioplasty in a representative coronary bifurcation. Journal of applied physiology (Bethesda, Md : 1985). 2010;109(2):532-40.

43. Taylor CA, Figueroa CA. Patient-Specific Modeling of Cardiovascular Mechanics. Annual Review of Biomedical Engineering. 2009;11:109-34.

44. Dean WR. Note on the motion of fluid in a curved pipe. London, Edinburgh, and Dublin Philosophical Magazine and Journal of Science. 1927;4(20):208-23.

45. Berger SA, Talbot L, Yao LS. Flow in Curved Pipes. Annual Review of Fluid Mechanics. 1983;15(1):461-512.

46. Pedley TJ. The fluid mechanics of large blood vessels. Cambridge; New York: Cambridge University Press; 1980.

47. Siggers JH, Waters SL. Steady flows in pipes with finite curvature. Physics of Fluids. 2005;17(7):77102.

48. Van Canneyt K, Morbiducci U, Eloot S, De Santis G, Segers P, Verdonck P. A computational exploration of helical arterio-venous graft designs. Journal of Biomechanics. 2013;46(2):345-53.

49. Qiao AK, Guo XL, Wu SG, Zeng YJ, Xu XH. Numerical study of nonlinear pulsatile flow in S-shaped curved arteries. Medical engineering & physics. 2004;26(7):545-52.

50. Xie X, Wang Y, Zhou H. Impact of coronary tortuosity on the coronary blood flow: a 3D computational study. Journal of biomechanics. 2013;46(11):1833-41.

51. Alastruey J, Khir AW, Matthys KS, Segers P, Sherwin SJ, Verdonck PR, et al. Pulse wave propagation in a model human arterial network: Assessment of 1-D visco-elastic simulations against in vitro measurements. Journal of Biomechanics. 2011;44(12):2250-8.

52. Dean WR. LXXII. The stream-line motion of fluid in a curved pipe (Second paper). Philosophical Magazine Series 7. 1928;5(30):673-95.

53. Chien S. Effects of disturbed flow on endothelial cells. Ann Biomed Eng. 2008;36(4):554-62.

54. Caro CG. Discovery of the role of wall shear in atherosclerosis. Arteriosclerosis, thrombosis, and vascular biology. 2009;29(2):158-61.

55. Himburg HA, Grzybowski DM, Hazel AL, LaMack JA, Li X-M, Friedman MH. Spatial comparison between wall shear stress measures and porcine arterial endothelial permeability. American Journal of Physiology - Heart and Circulatory Physiology. 2004;286(5):H1916-22.

56. Caro CG, Cheshire NJ, Watkins N. Preliminary comparative study of small amplitude helical and conventional ePTFE arteriovenous shunts in pigs. Journal of The Royal Society Interface. 2005;2(3):261-6.

57. Gallo D, Steinman DA, Bijari PB, Morbiducci U. Helical flow in carotid bifurcation as surrogate marker of exposure to disturbed shear. Journal of biomechanics. 2012;45(14):2398-404.

2 Effects of vessel tortuosity on coronary hemodynamics: an idealized and patient-specific computational study*

Natalya Vorobtsova[1], Mark Stremler[2], David Sane[3], Francesco Migliavacca[4], Claudio Chiastra[4], Pavlos Vlachos[5]

[1]Department of Mechanical Engineering, Virginia Tech, Blacksburg, Virginia, USA

[2]Department of Engineering Science and Mechanics, Virginia Tech, Blacksburg, Virginia, USA

[3]Section of Cardiology, Carilion Clinic, Virginia Tech Carilion School of Medicine, Roanoke, Virginia, USA

[4]Laboratory of Biological Structure Mechanics (LaBS), Chemistry, Materials and Chemical Engineering Department 'Giulio Natta', Politecnico di Milano, Milan, Italy

[5]School of Mechanical Engineering, Purdue University, West Lafayette, Indiana, USA

2.1 Abstract

A phenomenon of coronary tortuosity is believed to significantly influence hemodynamics inside coronary arteries. However, a correlation between tortuosity and flow alterations is not well investigated due to the lack of patient-specific studies and an absence of a clear definition of tortuosity. A computational investigation of how tortuosity affects flow parameters, such as pressure drop, wall shear stresses, strength of helical flow, measured by helicity intensity, and concomitant risks was performed. An idealized study considered three simplified curved vessels with zero-torsion to model tortuous arteries. A patient-specific study was based on real coronary vessels obtained from clinical data, and a statistical analysis was performed. Results indicate that a risk of perfusion defects grows with an increased degree of tortuosity due to an increased pressure drop. Unlike the results of idealized study, real tortuous arteries showed to be less prone to atherosclerosis. Thereby, modeling of coronary tortuosity should account for all aspects of tortuosity including a heart shape that introduces additional torsion. Moreover, helicity intensity is shown to depend strongly on tortuosity and affect flow alterations and accompanying disease risks. It might help in developing a universal parameter to describe tortuosity and assess its impact on the health of a patient.

* Will be in revision for Annals of Biomedical Engineering

2.2 Introduction

Coronary arteries are the blood vessels that supply oxygen-rich blood to the myocardium. Tortuous epicardial coronary vessels take abnormally curved or helically coiled paths that may have turns and loops (1-5). These may lead to flow alterations that can cause reduced blood supply to the heart tissues during exercise and lead to ischemia (2). Clinical and experimental evidence show that tortuosity can develop due to mechanical factors such as transmural pressure (6), blood pressure (7, 8), blood flow(9), axial tension (10), and wall structural changes (1, 7).

Although cardiologists often encounter coronary tortuosity, its mechanisms and impacts are not well studied. It is well-known that coronary tortuosity is often correlated with such clinical conditions as coronary artery disease (1), diabetes (11), myocardial infarction (3), hypertension (12), and age (2-4, 12, 13). However, even when no other diseases or abnormalities are present, tortuosity can cause various dysfunctions. While mild tortuosity of coronaries is often asymptomatic, severe tortuosity may lead to angina pains during exercise, a positive stress test, or a myocardial ischemic attack (1, 14).

Tortuosity can be quantified using various tortuosity metrics such as the distance metric or the relative length variation (1, 11, 15-19), the inflection count metric (11), the sum of angles metric (11), the total torsion (20) and the total curvature (17, 20), the average torsion (15) and the average curvature (15), the total squared curvature(17), and the normalized root-mean squared curvature (8). All of these metrics represent different aspects of tortuosity. Some of them have been found appropriate for specific types of tortuosity; for example, the sum of angles metric was shown to be good for measuring the tortuosity of tight low-amplitude coils, while the distance metric and inflection count metric are good for characterizing vessels with broad meandering curves (11).

The curvature-dependent forces and torsional forces were found to drive secondary motions of the flow (21). Curvature generates motions in the normal to the axial direction (22), firstly investigated by Dean (23), creating helical motions of the flow. The pressure drop in the idealized curved pipe was also found to be larger than the pressure drop for the same flow rate in the corresponding straight pipe of the same length (24, 25). Torsional forces break the symmetry of the curvature-generated helical motions making one helical structure more dominant (21). The pressure drop required to drive the blood through an idealized helically coiled pipe was found to

grow with number of helical coils for the same length of the vessel (26). Patient-specific numerical simulations of Xie *et al*. (27) have shown that the resistance to the blood flow increases in the presence of tortuosity in coronary arteries.

Atherosclerotic lesions are believed to appear in the regions of low or oscillatory wall shear stress (WSS), or, as we denote it, the regions of "disturbed" WSS (28). As the coronary tortuosity and tortuosity in general is not well defined in literature and not well understood, it is difficult to draw definite conclusions about the influence of tortuosity on susceptibility of arteries to atherosclerosis, especially considering a very limited number of patient-specific studies. Moreover, some contradiction exists about a development of atherosclerosis in tortuous coronary arteries. A clinical study of Li *et al.* shows that coronary tortuosity may have suppressing effect on atherosclerosis (29). At the same time, a numerical study of Xie *et al.* reports that severe coronary tortuosity may lead to atherosclerosis (27, 30). We think that inconsistency in results may be due to the fact that the numerical model may be too simplified, and some aspects of coronary tortuosity were not taken into account, it is also possible that the tortuosity degree defined in the clinical study does not consider all of the important aspects of tortuosity. Theoretical, experimental, and numerical investigations of different aspects of tortuosity, such as flow in the bends of constant curvature (23, 24, 31, 32), helically coiled pipes of constant curvature and torsion (24, 26), idealized helical arterio-venous graft designs (33), S shaped pipes with planar centerline (21, 30, 34) and with torsion (21, 35), and two subsequent S-shaped vessels (21) were carried out over the years and have shown that different aspects have different impact on the WSS distribution. For example, a numerical investigation of the flow in a curved pipe without torsion showed to lead to a larger region of disturbed WSS (30). Torsion, on the other hand, leads to a more complex flow field that reduces the area zones exposed to atherogenous conditions (33). Besides, torsion leads to a more uniform spatial distribution of the WSS (22), which, according to Caro *et al.* (36), reduces the risk of vessel occlusion. In fact, real arteries have specific configurations and can include various aspects of tortuosity which can lead to different conclusions on the WSS distribution. Thus, clinical and numerical studies showed that tortuosity of femoral arteries may cause atherosclerosis (16, 18), while Gallo's *et al.* (15) recent numerical study demonstrated tortuosity of carotid bifurcation to be atheroprotective. Overall, to elucidate this problem, first, an appropriate parameter describing and unifying all

aspects of the coronary tortuosity is required. Second, a statistical approach is necessary to understand a correlation between tortuosity and WSS distribution.

Our analysis aims to explore the dependence of the flow parameters on the tortuosity of the vessel and investigate a correlation between tortuosity, pressure drop, and wall shear stress distribution for idealized and patient-based geometries. In the idealized study, we focus on the influence of curvature without torsion on the flow in the vessel. In contrast to previous works (21, 30, 34), the curved coils have decreasing amplitude of each subsequent coil, and the vessel has a uniform tapering, thus providing better physiological fidelity. The geometric parameters, such as the number of coils, the amplitude of coils, and the tapering coefficient were obtained from clinical data. The patient-specific analysis is based on three cases, and the post processing is made for each vessel segment of coronary vessel trees, resulting in 23 vessel segments allowing for statistical analysis of the coronary tortuosity. We also show a dependence of the strength of helical flow in an artery on the degree of tortuosity and its significant impact on pressure drop and WSS distribution. We discuss that the helicity intensity of the helical flow might present a good way to describe tortuosity and serve as a universal parameter to investigate flow alterations and accompanying risks to health.

2.3 Materials and methods

2.3.1 Geometrical models

2.3.1.1 Idealized study

Idealized 3D geometries of tortuous coronary vessels were modeled. Since the aim of the idealized study is to compare flow parameters of vessels with a different number of curved arcs, but without torsion and branching, the centerline of the vessel geometries lies on a plane, and bifurcations are not considered. We denote cases as T-5, T-6, and T-7 (Figure 2 a–c), where the numeric signifies the number of curved arcs. The amplitude of each subsequent bend is smaller than that of the previous bend. All cases have an inlet radius of 1.5 mm and a uniform tapering of the vessel, with the inlet radius twice the size of the outlet radius.

2.3.1.2 Patient-specific study

High-resolution Computed Tomography Angiograms (CTA)† for three patients (patient-A, -B, and -C) were used to build the 3D geometries. The left coronary artery tree was segmented from each CTA using ITK-SNAP (37). The resulted segmentation was manually improved in those locations where the automatic segmentation failed, smoothed, and exported to CAD using MeshLab (38) and Geomagic Studio® (3D Systems, Cary, NC, USA). The resulting geometries for all three cases are shown in Figures 1 (d-f).

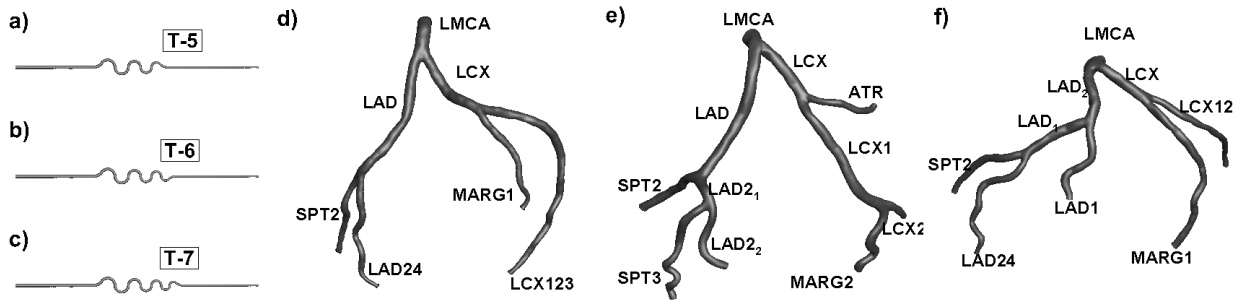

Figure 2. Geometries for the idealized and patient-specific studies. Geometries for the idealized study: vessel model with (a) 5, (b) 6, and (c) 7 curved arcs. Geometries for the patient-specific study: patient-A (d), patient-B (e), patient-C (f). A name of each branch for patient-specific geometries is indicated next to it.

2.3.2 Geometric characterization of vessel segments

2.3.2.1 Vessel centerline extraction

In this study we focus on investigating the relationship between flow parameters and degree of tortuosity. In the post-processing of a solution of an idealized case, straight parts at the beginning and end of the vessel are excluded as shown in Figure 2 (a). Horizontal coordinates of points P_1 and P_2 are at the same distance from the inlet of the vessel for all cases. For the post-processing of patient-based cases, bifurcating regions are excluded, and each vessel tree is split into individual segments as shown in Figure 3 (b). Splitting the three patient-specific cases gives us 23 vessel segments, which, in contrast to the idealized cases, allow us to perform a statistical analysis of the solution.

† Clinical data for the study is provided by the research group of David Sane at Carilion Cardiology Clinic, Roanoke, VA

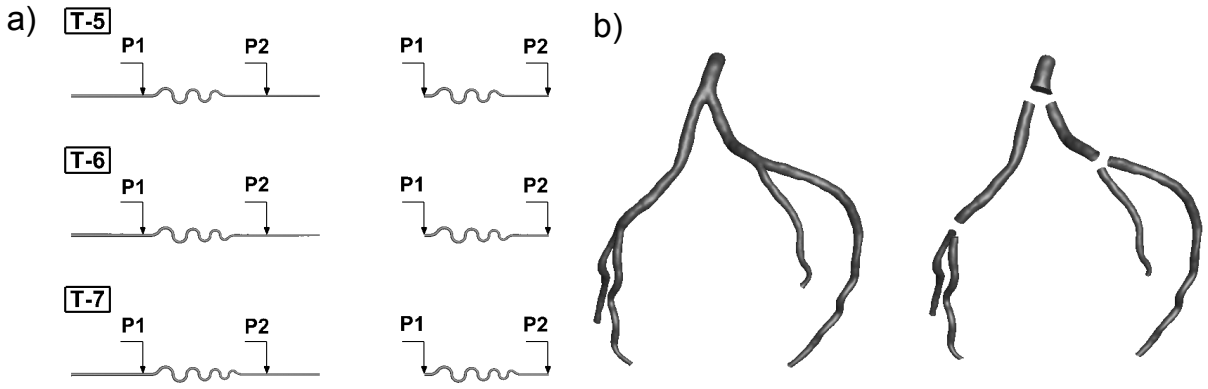

Figure 3. (a) Idealized geometry segments considered in the post-processing of the solution. (b) An example of splitting of the vessel tree for patient-A.

A geometric analysis of each vessel segment geometry is done by analyzing the centerline of the segment (19, 20, 39-42). For patient-based cases, tracking of the centerline is performed by dividing each branch into cross-sections 0.8 mm apart and connecting its center points. A centerline of a vessel segment is then described as a parametric curve by means of a curvilinear variable *s*:

$$\gamma(s) = \left(x(s), y(s), z(s)\right) . \tag{1}$$

The centerline deviation from a straight line at each point of the curve can be measured by curvature (κ):

$$\kappa(s) = \frac{\left|\gamma'(s) \times \gamma''(s)\right|}{\left|\gamma'(s)\right|^3} . \tag{2}$$

Torsion (τ), a measure of how sharply the curve is twisting out of the plane of curvature, is calculated as:

$$\tau(s) = \frac{\left(\gamma'(s) \times \gamma''(s)\right) \cdot \gamma'''(s)}{\left|\gamma'(s) \times \gamma''(s)\right|} . \tag{3}$$

To reduce high-frequency noise from the segmentation and the centerline tracking process and allow for a geometric characterization of the centerline, a local fifth-order polynomial filter with Gaussian kernel is applied to each coordinate (19, 41).

2.3.2.2 Tortuosity metrics

In order to characterize the degree of tortuosity, we use the following metrics. The distance metric (DM) quantifies the "lengthening effect" of tortuosity (1, 11) and is a very common way to measure tortuosity:

$$DM = \frac{L}{l}, \tag{4}$$

where L is the path of the centerline, and l is the distance between the beginning and end.

The total curvature (TC) and the total torsion (TT) metrics are calculated by an integration of the curvature and the absolute value of torsion along the centerline, respectively (16, 17, 20, 40):

$$TC = \int_0^L \kappa(s)\, ds \ , \tag{5}$$

$$TT = \int_0^L \left|\tau(s)\right| ds \ . \tag{6}$$

2.3.3 Computational fluid dynamics modeling

2.3.3.1 Boundary conditions and simulation settings

Pulsatile fluid dynamic simulations are carried out by means of the finite volume solver ANSYS Fluent 14.5 (ANSYS Inc., Canonsburg, PA, USA). At the inlet, a uniform velocity profile is used, with the axial velocity following the representative velocity in the left anterior descending artery (LAD) for the idealized cases and in the left main coronary artery (LMCA) for the patient-specific studies (43). The average flow rate is adjusted for each patient-specific case according to van der Giessen e*t al.* (44):

$$q = 1.43 d^{2.55} \ , \tag{7}$$

where q is the flow rate and d is the diameter of the inlet. The outlet boundary condition for the idealized cases is taken to be constant pressure. The outlet boundary condition for the patient-specific cases is given by a lumped parameter model, the resistance boundary condition, with the outlet pressure calculated at each time step as:

$$p(t) = R \cdot q(t) \ , \tag{8}$$

where R is the resistance of the entire downstream vascular system. The resistance values are adopted from Pietrabissa *et al.* (45). The no-slip boundary condition is applied to the vessel wall, which is considered rigid. The blood density is constant and equal to 1060 $kg\ m^{-3}$, and the Carreau model (46) is used to model the non-Newtonian behavior of the blood. The flow is assumed to be laminar. A coupled solver is used with a second-order upwind scheme for the momentum spatial discretization and second-order implicit scheme for time. A convergence criterion is set to give the relative error of the solution parameters from the converged solution to be less than 0.01%. For idealized and patient-specific cases, 100 and 800 time steps per cardiac cycle are set, respectively. Three cardiac cycles are calculated to ensure the periodicity of the solution. Coupled grid and time sensitivity analysis is performed. For the patient-specific cases, coarse, medium, and fine meshes are considered with 1487340, 702440 and 3045176 elements and 440, 600, and 800 time steps per cardiac cycle, respectively. The relative discretization error for the fine mesh does not exceed 0.1% for selected pressure- and wall-shear-dependent flow parameters.

2.3.4 Quantification of the results

Assessing the reduction in the pressure downstream the tortuous vessel segment is important because it may lead to a decreased perfusion. Therefore, one of the main parameters of interest is the time-averaged difference between the area-weighted average of the pressure values at the entrance and exit to the vessel segment per unit length $\frac{\Delta P}{L}$. Normalizing the pressure drop by the length of the vessel removes a contribution due to friction losses caused by the length of the vessel. To compare results of idealized and patient-specific studies, $\frac{\Delta P}{L}$ in the idealized study is non-dimensionalized by the pressure drop per unit length for an equivalent non-tortuous vessel of the same total length. For patient-specific cases, it is non-dimensionalized by the viscous scale (47).

Both experimental (48) and theoretical (23, 49) studies have shown that curvature and torsion contribute to the initiation and development of helical patterns in the flow. To help visualize the

flow patterns inside tortuous vessels, we calculate the local normalized helicity (LNH), which describes an interplay between rotational and translational motion (15, 33, 50-53):

$$LNH = \frac{\left(\nabla \times v\right) \cdot v}{\left|\nabla \times v\right| \cdot \left|v\right|} = \cos\alpha \ , \tag{9}$$

where α is the angle between the velocity v and the vorticity ($\nabla \times v$). Positive or negative values indicate clockwise and counter-clockwise rotating fluid structures along the flow direction, respectively. We also consider the helicity intensity of the flow:

$$h_2 = \frac{1}{T\Omega} \int_0^T \int_\Omega \left|\left(\nabla \times v\right) \cdot v\right| d\Omega dt \ , \tag{10}$$

where Ω is the volume of the vessel segment and T is the duration of a cardiac cycle (15, 50).

Calculating the LNH helps to realize flow patterns inside a vessel (15, 33, 50-53), while helicity intensity h_2 is an indicator of the strength of a helical flow in the domain (15, 50). Previous studies have shown that for carotid bifurcations h_2 is curvature-driven, and its high values are instrumental in suppressing disturbances of the WSS distribution (15, 50). The h_2 can be non-dimensionalized as follows:

$$\frac{h_2 \cdot L}{V^2} \ . \tag{11}$$

In order to study the dependence of the flow parameter h_2 on the degree of tortuosity, we perform a series of calculations to evaluate the helicity intensity in each vessel. A correlation between geometry of a vessel segment and the helical flow in it is investigated by forming a regression of the helicity intensity, h_2, versus the tortuosity metrics DM, TT, and TC.

Another essential physical quantity for this study is the distribution of wall shear stress, which we evaluate in terms of the time averaged wall shear stress (TAWSS) distribution (54). Areas of the vessel wall with low TAWSS (smaller than 0.5 Pa) have been shown to correlate with a higher risk for atherosclerosis (55, 56). This correlation might be explained by an increased uptake of the blood-borne particles in the areas of low WSS to the wall which is prevalent in atherosclerosis (57). The risk may increase if the particle stays near the wall for a longer time. Residence times of particles near the wall can be evaluated with the help of a relative residence

time (RRT) (58). Regions of high RRT are regions near the wall where a particle moves slower than in a region of low RRT. Coupled with low TAWSS, such regions are associated with an increased risk of coronary artery disease (59). Hereafter, we call the regions of low TAWSS and high RRT the regions of "disturbed WSS". Following Lee *et al.* (60, 61), we characterize the TAWSS and RRT distributions for each vessel segment by two threshold values for which 90% of the vessel segment surface is exposed to higher TAWSS and lower RRT than corresponding TAWSS and RRT thresholds. Those thresholds are denoted as TAWSS90 and RRT90.

2.4 Results

2.4.1 Idealized study

The metric values and other geometric descriptors, such as average radius, average tapering, and length of the vessel segment, are presented in Table 1 for three idealized cases (T-5, T-6, and T-7). Results indicate that DM and TC grow with the number of curved arcs.

Table 1. Values of geometric descriptors for three idealized cases (T-5, T-6, T-7). Descriptors are calculated for the part of the geometry between points P_1 and P_2. Geometric descriptors: distance metric (DM), total torsion (TT), total curvature (TC), length, average radius (Rave) and average tapering coefficient (Tave).

	Length (mm)	Rave (mm)	Tave (arb. units)	DM (arb. units)	TT (arb. units)	TC (arb. units)
T-5	127.9229	1.125	0.5	1.279	0	17.055
T-6	131.1199	1.125	0.5	1.311	0	20.043
T-7	134.9229	1.125	0.5	1.349	0	22.844

Figure 4 (a) shows that the dimensionless pressure drop per unit length for the tortuous part of the main vessel increases with the number of curved segments, i.e. the tortuosity degree of the main vessel. That signifies that a more curved vessel requires larger flow driving force. Figure 4 (b) also shows that the helicity intensity is higher for the cases with a larger number of curved segments. In addition, results indicate that a more tortuous vessel has a lower TAWSS90 and

higher RRT90 (Figure 4 c-d) meaning that such a vessel has a larger area of lower TAWSS and a larger area of higher RRT, and, as result, the WSS distribution is more disturbed in that region. It is evident that, while helicity intensity changes significantly with the number of arcs, flow parameters difference is only about 5%. However, as we are investigating simple geometries in this part of the study, our goal is to explore dependencies rather than absolute values of parameters, and we observe a clear effect of the number of curved arcs on the flow parameters. In the next section, the results of patient-specific study are presented where a statistical analysis is performed for 23 real coronary vessels in order to further investigate the correlation between degree of tortuosity and flow parameters.

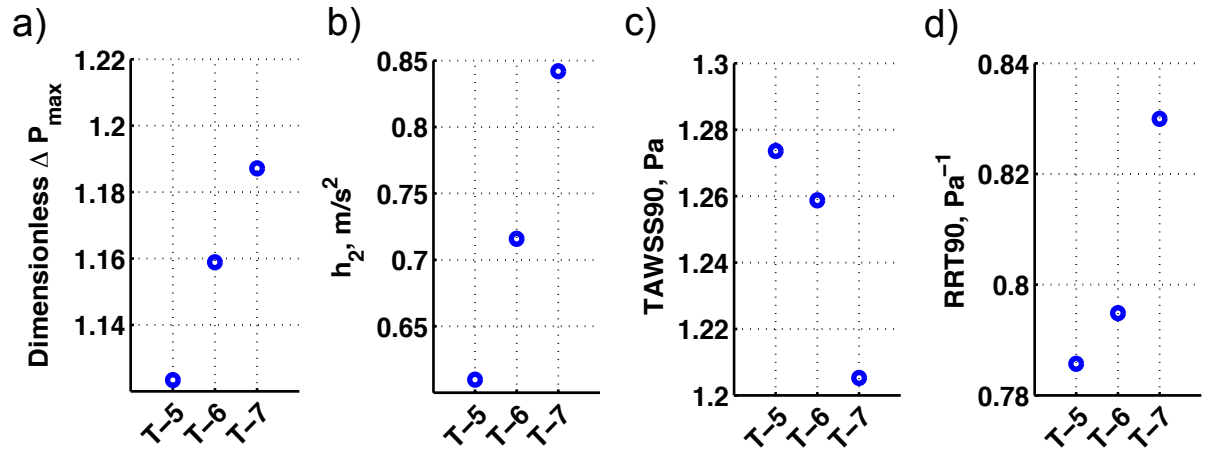

Figure 4. (a) Dimensionless pressure drop for the idealized cases. (b) Helicity intensity h2 for idealized cases. (c) Threshold of TAWSS for which 10% percent of the area has lower TAWSS for idealized cases. (d) Threshold of RRT for which 10% percent of the area has higher RRT.

2.4.2 Patient-specific study

2.4.2.1 Relation between tortuosity metrics

The metric values and other geometric descriptors, such as average radius, average tapering, and length of the vessel segment, are presented for three patient-specific cases in Table 2.

Table 2. Values of geometric descriptors for 23 vessel segments obtained from three patient-specific cases (patient-A, patient-B, patient-C). Geometric descriptors: distance metric (DM), total torsion (TT), total curvature (TC), length, average radius (Rave), and average tapering coefficient (Tave). Bold denotes maximum value of the geometric descriptor among the vessel segments for one patient

		Length (mm)	Rave (mm)	Tave (arb. units)	DM (arb. units)	TT (arb. units)	TC (arb. units)
Patient-A	LMCA	7.881	2.540	1.006	1.009	4.778	0.714
	LAD	42.764	1.798	1.000	1.054	12.071	1.717
	LAD24	41.502	1.192	0.970	1.114	15.262	4.592
	LCX	25.683	1.920	0.590	1.053	6.159	1.523
	LCX123	84.027	1.429	1.005	**1.344**	**26.841**	**5.297**
	MARG1	37.648	1.152	0.456	1.059	9.530	3.274
	SPT2	33.394	1.148	0.400	1.041	8.497	2.257
Patient-B	LAD	33.465	1.557	1.001	1.031	7.169	1.723
	LAD2_2	16.402	1.085	0.490	**1.200**	6.133	2.495
	LCX	13.651	1.607	0.411	1.010	5.754	0.970
	LCX1	36.428	1.362	0.999	1.070	11.515	2.253
	ATR	18.994	0.917	0.514	1.133	5.327	2.296
	MARG2	18.742	1.170	0.508	1.173	8.520	5.368
	SPT2	18.626	1.128	0.527	1.030	8.163	1.177
	SPT3	30.647	1.022	0.858	1.123	**14.275**	**6.526**

	LAD_1	17.574	1.998	0.998	1.045	5.831	1.366
	LAD_2	20.874	2.062	1.006	1.015	9.463	0.885
	LAD1	26.893	1.564	1.006	1.170	7.078	3.383
	LAD24	43.672	1.295	1.006	**1.228**	**16.677**	**5.732**
	LCX	18.675	1.933	0.411	1.014	8.117	0.805
	LCX12	54.162	1.238	1.003	1.109	9.175	2.186
Patient-C	MARG1	63.429	1.696	1.004	1.180	13.520	3.472
	SPT2	34.560	1.523	0.540	1.043	9.435	1.717

Figure 5 (a) demonstrates a scatterplot of the total torsion plotted versus corresponding total curvature that shows a varying severity of non-planarity and curvature of the left coronary arteries. It is worth noting that the total torsion for any of the 23 vessel segments does not get lower than a certain level of approximately 4.7, which means that all of the vessels exhibit substantial torsion. There is also a weak positive correlation between the total torsion and total curvature for these vessels as shown by the linear regression with $R^2 = 0.45$.

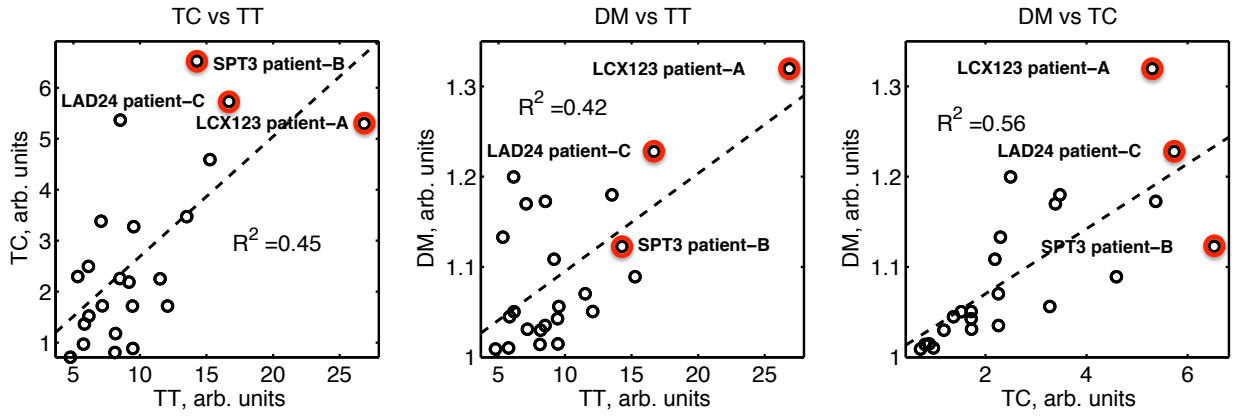

Figure 5. A scatter plot of the Total Torsion (TT) as a function of the Total Curvature (TC) (a), Distance Metric (DM) against the corresponding TT (b), DM against the corresponding TC (c) for 23 vessel segments. The black dotted line represents the linear regression fit. The three red circles indicate the data points for the branches LCX123 for patient-A, SPT3 for patient-B, and LAD24 for patient-C.

The lengthening of a vessel affects the curvature and torsion of the vessel and vice versa. Indeed, our results show a positive correlation between DM and TT and TC with R^2=0.42 and R^2=0.56 respectively as shown in Figure 4 (b) and (c).

2.4.2.2 Flow Patterns

The flow patterns of three representative cases are shown in Figures 5, 6 and 7. The corresponding vessels are indicated by red circles in Figure 5 and belong to three different patients. Two of three vessels (patient-A, patient-C) do not have a pronounced helically coiled shape, and its torsion is mainly due to the curvature of the heart. On the other hand, the vessel of patient-B has torsion due to a significantly helically coiled shape. For the characteristic vessel segment of patient-A (Figure 6 a), we chose three cross-sections along the curved bend (Figure 6 c). To assess the profile of the axial flow, the axial velocity magnitude is plotted on each of them as shown in Figure 5 (d-f). The WSS distribution is also shown for the branch (Figure 6 g). The LNH iso-surface visualization (LNH=+-0.4) from two angles of view is used to highlight the presence of helical structures and show its shape inside the branch as shown in Figure 6 (h). Similarly, the graphs visualizing the flow inside the characteristic branch of the patient-B and patient-C are shown in Figure 7 and 7.

We observe helical counter-rotating structures in multiple regions of the vessel tree. It may be explained by the fact that these regions have higher values of parameter K, first introduced by Dean (23, 62), than in the rest of the vessels. It was shown that secondary flow is dependent on this parameter (32, 48). For very small values of K, the flow can be approximated as a Poiseuille flow; with increasing K secondary flow velocities also increase. The maximum of K is 123.98 for patient-A, 148.33 for patient-B, 352.36 for patient-C, so we expect only two vortex structures to appear (32).

Flow visualization of the characteristic branch of patient-A (Figure 6 d-f) and patient-C (Figure 8 d-f) shows that the velocity profiles are skewed towards the outer side of the distal part of the bend. Regions of local maximum of the WSS are also located on the outer side of the distal part of the bend (Figure 6 g, Figure 8 g). The same trend is observed for the vessel of patient-B as can be seen in Figure 7 (d-f) and (g). The positioning and intensity of the velocity peak and the WSS distribution are dependent on the vessel geometry. All three vessels show helical structures in the curved parts of the vessel as depicted in Figure 6 (h), Figure 7 (h) and Figure 8 (h). For patient-A

and patient-C, these helical structures are relatively symmetric, while for patient-B a clock-wise rotating structure becomes much more dominant.

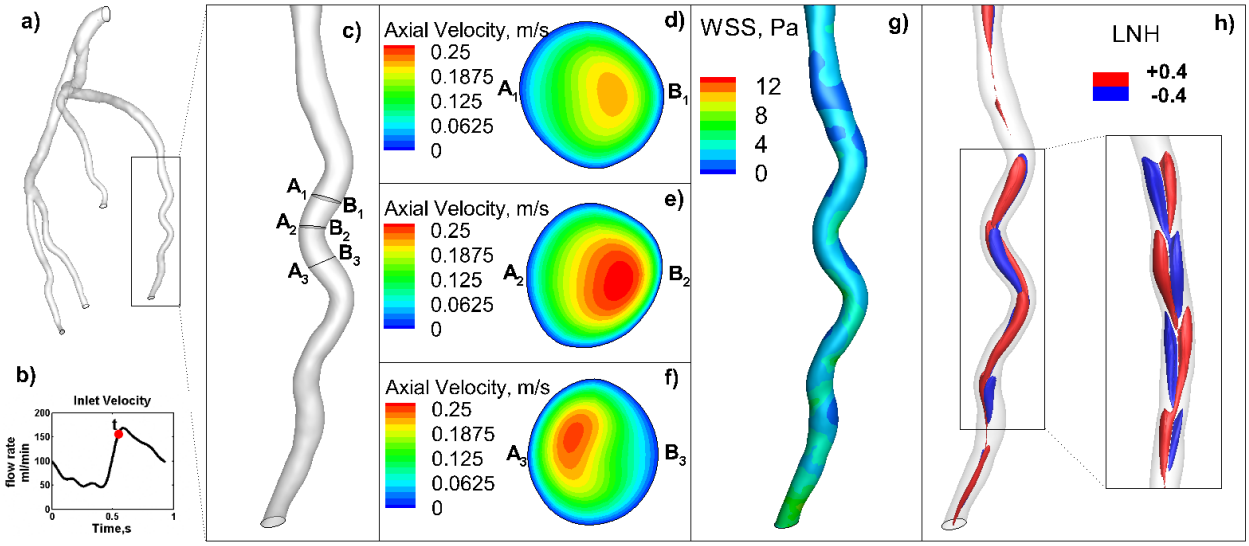

Figure 6. A solution for LCX123 branch of patient-A (shown is the part of the LCX123 with high total curvature and low total torsion) at time t = 0.558 s: (a) vessel tree geometry for patient-A; (b) flow rate at the inlet; the red dot indicates the flow rate at t = 0.558 s; (c) position of three cross-sections; (d-f) axial velocity magnitude for three cross-sections; the view of the cross-sections is from the downstream side of the cross-section; (g) wall shear stress distribution on LCX123; (h) iso-surface of LNH = ±0.4.

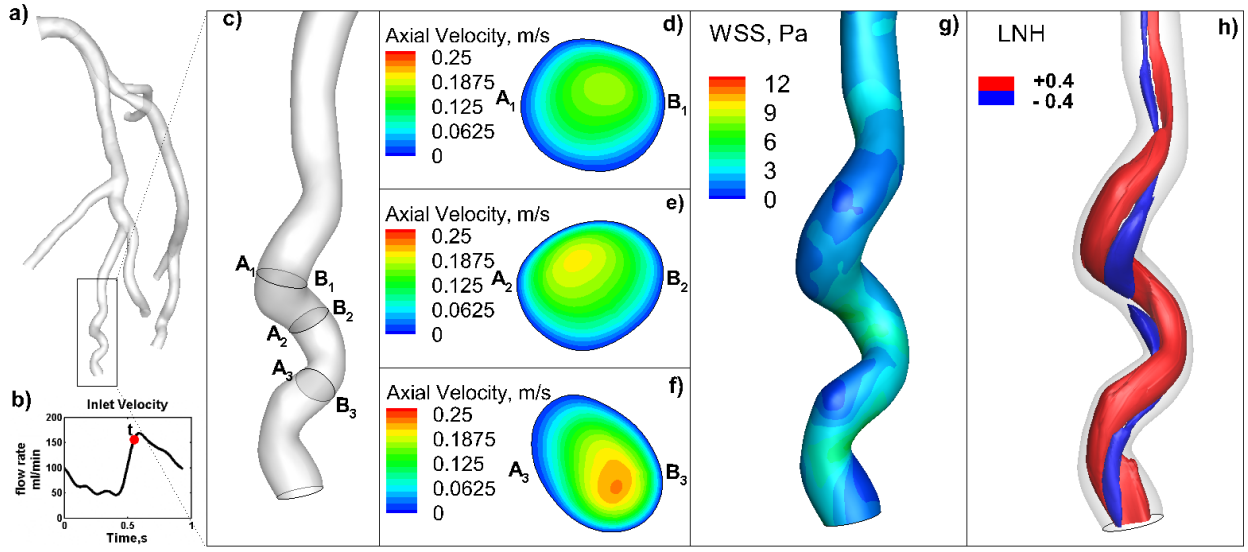

Figure 7. A solution for SPT3 branch of patient-B (shown is the part of the SPT3 with high total curvature and high total torsion) at time t = 0.558 s: (a) vessel tree geometry for patient-B; (b) flow rate at the inlet; the red dot indicates the flow rate at t = 0.558 s; (c) position of three cross-sections; (d-f) axial velocity for three

cross-sections; the view of the cross-sections is from the downstream side of the cross-section; (g) wall shear stress distribution on SPT3; (h) iso-surface of LNH = ±0.4.

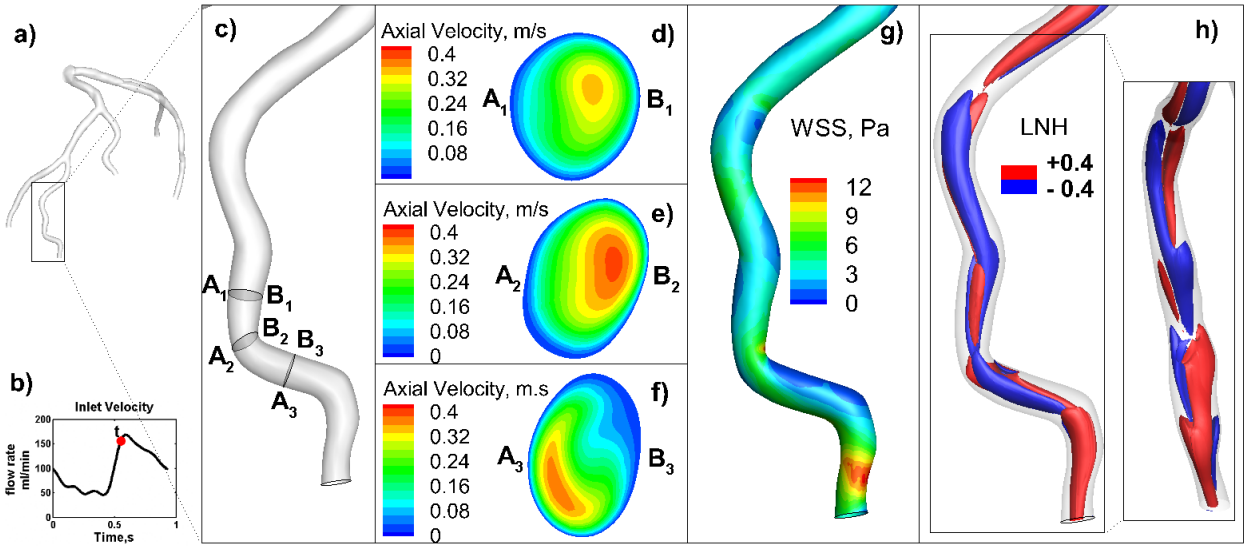

Figure 8. A solution for LAD24 branch of patient-C (shown is the part of the LAD24 with high total curvature and high total torsion) at the time t = 0.558 s: (a) vessel tree geometry for patient-B; (b) flow rate at the inlet; the red dot indicates the flow rate at t = 0.558 s; (c) position of three cross-sections; (d-f) axial velocity for three cross-sections; the view of the cross-sections is from the downstream side of the cross-section; (g) wall shear stress distribution on LAD24; (h) iso-surface of LNH = ±0.4.

In the patient-specific study, we try to show a direct statistical dependence between the tortuosity metrics and flow parameters. The results show a weak correlation between these parameters when simple logarithmic and linear regressions are used. Similarly to Gallo *et al*. studies on carotid bifurcations (15, 50), we investigate how the strength of the helical flow depends on tortuosity and if flow parameters of interest are affected by it. Figure 9 shows that a statistically significant dependence of the helicity intensity on TC is found (R^2 = 0.7); slightly weaker correlations are observed for DM (R^2 = 0.55) and TT (R^2 = 0.58). In all cases the helicity intensity is positively correlated with tortuosity metrics. That indicates that a larger tortuosity of a vessel causes a higher intensity of the helical flow. We also considered how the asymmetry, or the balance, between the counter-rotating helical structures, expressed by a parameter h_4 introduced by Gallo *et al.* (50), is related to the tortuosity metrics. However, our calculations did not yield any significant dependence between these parameters.

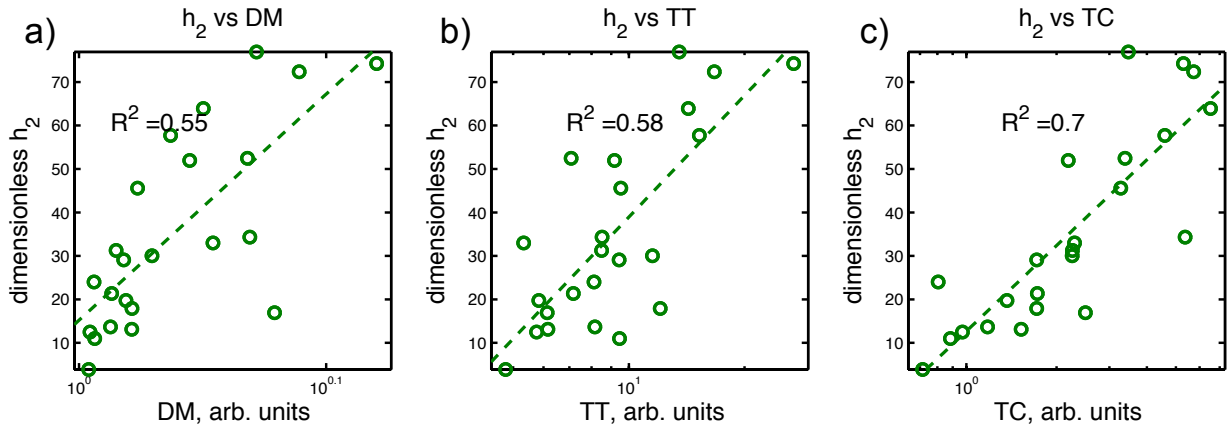

Figure 9. Scatter plots showing the helicity intensity h2 calculated for each of 23 vessel segments versus the tortuosity metrics DM (a), TT (b), and TC (c). The dotted line shows the xlog regression fit, and R2 is the determination coefficient.

It is yet unclear how the pressure drop and WSS change when the flow in the vessel becomes more helical due to the tortuosity. To elucidate that problem, we investigate a correlation between flow parameters of interest and the helicity of the flow for each vessel. Figure 10 demonstrates the results of calculations performed to clarify a dependence of the pressure drop per unit length, TAWSS90, and RRT90 for all segments versus helicity intensity h_2. The plots show an obvious positive correlation of the dimensionless pressure drop per unit length and dimensionless helicity h_2 with $R^2 = 0.67$ (Figure 10 a), positive correlation of TAWSS90 and h_2 with $R^2 = 0.62$ (Figure 10 b), negative correlation of RRT90 and h_2 with $R^2 = 0.73$ (Figure 10 c). In agreement with the results of the idealized case study, we observe a pronounced increase in the pressure drop per unit length of the vessel as the helicity intensity of the flow becomes larger in more tortuous vessel. However, unlike the observation of idealized cases, Figure 10 (b) and (c) show that the higher helicity intensity is a strong predictor to have a smaller area of the vessel with lower TAWSS and smaller area of large RRT.

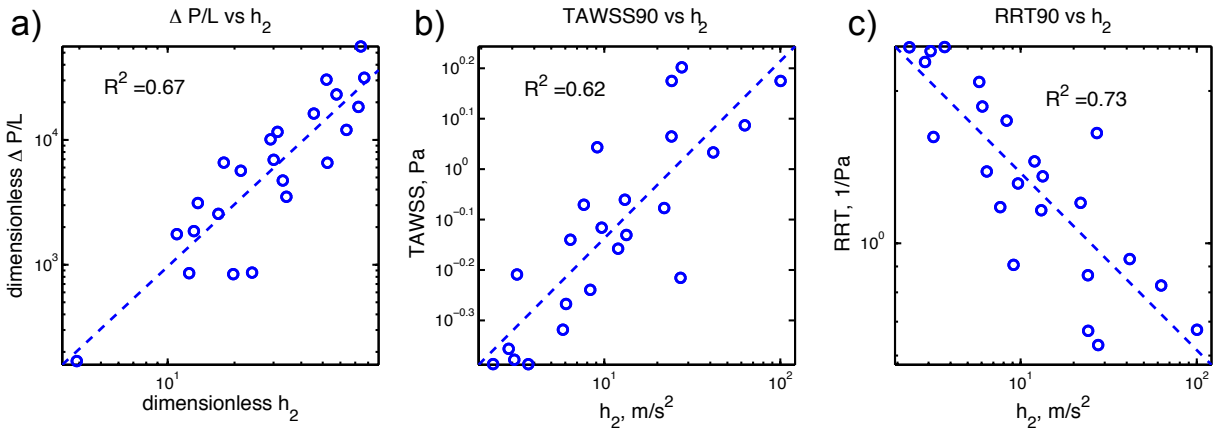

Figure 10. Scatter plots of the (a) dimensionless pressure drop per unit length calculated for each of 23 vessel segments versus corresponding dimensionless helicity intensity h2; (b) TAWSS90 calculated for each of 23 vessel segments versus corresponding helicity intensity h2; (c) RRT90 calculated for each of 23 vessel segments versus corresponding helicity intensity h2. The dotted lines shows the loglog regression fit to the scatter points. R2 is the determination coefficient. In contrast to the non-dimensionalized pressure drop, we are interested in absolute values of the WSS parameters and we plot them versus the dimensional helicity intensity.

2.5 Discussion

In the literature tortuosity has been identified as a predictor of abnormal hemodynamics in coronary arteries leading to reduced perfusion due to a decreased pressure downstream the tortuous vessel (2, 14) and an increased risk of atherosclerotic diseases (1, 2, 30, 63, 64). The CFD has emerged as a powerful tool to elucidate some of these aspects.

The objective of the current study was to investigate how the pressure drop, WSS, and RRT hemodynamic descriptors are affected by different aspects of tortuosity such as curvature, torsion, and lengthening due to tortuosity. To fulfill this goal we performed calculations of the 3D idealized and patient-based geometries. The idealized geometries represented a simplified tortuous coronary artery without branches. They were designed to investigate the curvature aspect of tortuosity in the absence of torsion. The patient-specific models were built using segmentation of the vessels from the 3D coronary CT angiograms of the left coronary tree. We found out that a correlation exists between total curvature and torsion metrics, and that the torsion is present for each segment due to the shape of the heart.

Although we were unable to find a very pronounced linear or logarithmic relation between tortuosity metrics and flow parameters in study, our investigation showed that a more complicated relation between these parameters exists and can be expressed with the help of the helicity intensity of the flow in the vessel. First, the visualization of the flow indicated that the helical motion is very pronounced in tortuous vessels. Next, the results of calculations performed for both idealized and patient-based cases showed that there is a pronounced correlation between tortuosity degree and helicity intensity. We observed that an increasing tortuosity is a statistically significant predictor of the growing helicity intensity. Moreover, we became interested if the intensity of the helical flow in coronary arteries might have an impact on the flow parameters and investigated that correlation.

A relationship between tortuosity metrics, helicity intensity, and pressure drop per unit length indicated that tortuosity might cause a decreased perfusion that can lead to a reduced blood supply to tissues during exercise. The dimensionless pressure drop per unit length of the vessel was shown to be positively correlated with non-dimensional helicity intensity. Considering the positive correlation between tortuosity descriptors and the helicity intensity, we observed that,

for both the idealized and patient-specific cases, the pressure drop is growing as a function of tortuosity.

Previously, it has been reported that the regions exposed to high RRT and low TAWSS are more susceptible to the atherosclerotic lesion formation (28, 55). In this study we used parameters RRT90 and TAWSS90 defined as the higher 10-percentile threshold for RRT and lower 10-percentile threshold for TAWSS to assess TAWSS and RRT distributions. An increasing value of TAWSS90 suggests that the area of low TAWSS is getting lower. Similarly, a decreasing RRT90 value signifies a decreasing area of high RRT. Thus, if an artery has a high value of RRT90 and low value of TAWSS90, it will have a tendency to have disturbed WSS which is considered to be more prone to atherosclerosis.

A correlation between the WSS derived descriptors and tortuosity of the vessel was studied for both idealized and patient-specific cases. The results of the idealized-case study showed that an increasing degree of tortuosity makes the helicity intensity grow, while values of TAWSS90 and RRT90 decrease and increase respectively. Consequently, it may indicate that TAWSS90 and RRT90 are positively and negatively correlated with helicity intensity in the case of zero torsion. However, for the real patient-based cases, we observed that the non-dimensional helicity intensity showed an opposite correlation with the WSS derived descriptors. Thus, our result indicates that, when torsion is present, real tortuous artery vessels have strong helical blood flow and are less prone to atherosclerosis, as an area of low TAWSS and an area of high RRT decrease with increasing helicity intensity due to tortuosity. We attribute that discrepancy between results of a simple 3D case of zero-torsion geometry and a patient-based vessel to the fact that arteries with non-zero curvature in a real heart would also have significant torsion due to the heart shape.

One of the long standing goals of investigations devoted to coronary tortuosity is to define one parameter that would clearly describe how tortuous the vessel is and how flow parameters change with it. Then, it would be easy to categorize tortuous vessels and estimate possible risks of health problems related to tortuosity. Our study showed that different aspects of tortuosity, like torsion or curvature, have different impacts on results of calculations, and it is not possible to use a single tortuosity metric to describe it and draw any definitive conclusions about the coronary hemodynamics and concomitant risks. However, as our observation indicate, the

helicity intensity, on one hand, always strongly depends on the degree of tortuosity and, on the other hand, is a pronounced statistical predictor of flow alterations that cause pressure drop and WSS change. Thus, even though further investigations are required, we believe the helicity intensity might be an excellent universal parameter to define tortuosity and its impacts on the health of a patient.

We have to mention that the study has some limitations. First, due to resolution restrictions, the segmentation and smoothing of the patient-based geometries introduces errors. Next, for both the idealized and patient-specific studies, the wall of the vessel was considered to be rigid. In the patient-based study, myocardium was considered to be non-moving, and the influence of the displacement of myocardium during the cardiac cycle is neglected. The study can be improved by considering more complicated lumped parameter boundary conditions. Also, to get the full picture of the flow inside tortuous coronary arteries, it is important to consider an influence of the exercise regime of the flow on the increase of the pressure drop and WSS distribution. Despite the limited number of the investigated patient-specific cases, we believe that this study represents an important step to get insights into the coronary tortuosity and its relation to hemodynamics.

The findings of this study help realize that the tortuosity should be modeled by a sophisticated parameter which will include both curvature and torsion effect of the tortuosity. Two different sources of torsion, torsion due to the shape of the heart and torsion due to the acquired helical shape of the vessels, should be included. Overall, our study showed that the pressure drop in a coronary artery increases as a function of the tortuosity degree of the vessel, so the artery might be more prone to perfusion defects. In agreement with previous idealized studies of Xie *et al*. (30, 35), an investigation of idealized cases without torsion shows that tortuosity may increase the risk of atherosclerosis. At the same time, our patient-specific statistical analysis indicates that tortuosity decreases the risk of atherosclerosis, a result similar to observations of a clinical study of Li *et al.* (29) and a recent investigation of tortuosity of the carotid bifurcations (15, 50). This is an interesting and important result that signifies that tortuosity of coronary arteries, in some cases, might be used to counterbalance a risk of atherosclerosis in a patient that has other conditions leading to it. Our patient-specific study also indicates an importance of the strength of helical flow in tortuosity investigations. Overall, future investigations will help realize if helicity

intensity can be used as a universal tool to predict and fully elucidate benefits or adverse effects of coronary tortuosity on the health of a patient.

References

1. Han HC. Twisted Blood Vessels: Symptoms, Etiology and Biomechanical Mechanisms. Journal of Vascular Research. 2012;49(3):185-97.

2. Zegers ES, Meursing BTJ, Zegers EB, Ophuis AJMO. Coronary tortuosity: a long and winding road. Netherlands Heart Journal. 2007;15(5):191-5.

3. Hutchins GM, Miner MM, Bulkley BH. Tortuosity as an index of the age and diameter increase of coronary collateral vessels in patients after acute myocardial infarction. The American Journal of Cardiology. 1978;41(2):210-5.

4. Turgut O, Yilmaz A, Yalta K, Yilmaz B, Ozyol A, Kendirlioglu O, et al. Tortuosity of coronary arteries: an indicator for impaired left ventricular relaxation? The International Journal of Cardiovascular Imaging. 2007;23(6):671-7.

5. Barilla F, Romeo F, Rosano GMC, Valente A, Reale A. Coronary artery loops and myocardial ischemia. American Heart Journal. 1991;122(1):225-6.

6. Kylstra JA, Wierzbicki T, Wolbarsht ML, Landers rMB, Stefansson E. The relationship between retinal vessel tortuosity, diameter, and transmural pressure. Graefe's archive for clinical and experimental ophthalmology = Albrecht von Graefes Archiv für klinische und experimentelle Ophthalmologie. 1986;224(5):477-80.

7. Cheung CY-L, Zheng Y, Hsu W, Lee ML, Lau QP, Mitchell P, et al. Retinal vascular tortuosity, blood pressure, and cardiovascular risk factors. Ophthalmology. 2011;118(5):812-8.

8. Dougherty G, Johnson MJ, Wiers MD. Measurement of retinal vascular tortuosity and its application to retinal pathologies. Medical & Biological Engineering & Computing. 2010;48(1):87-95.

9. Sutter FKP, Helbig H. Familial retinal arteriolar tortuosity: A review. Survey of Ophthalmology. 2003;48(3):245-55.

10. Jackson ZS, Dajnowiec D, Gotlieb AI, Langille BL. Partial off-loading of longitudinal tension induces arterial tortuosity. Arteriosclerosis, thrombosis, and vascular biology. 2005;25(5):957-62.

11. Bullitt E, Gerig G, Pizer SM, Lin W, Aylward SR. Measuring tortuosity of the intracerebral vasculature from MRA images. IEEE transactions on medical imaging. 2003;22(9):1163-71.

12. Del Corso L, Moruzzo D, Conte B, Agelli M, Romanelli AM, Pastine F, et al. Tortuosity, kinking, and coiling of the carotid artery: expression of atherosclerosis or aging? Angiology. 1998;49(5):361-71.

13. Soikkonen K, Wolf J, Mattila K. Tortuosity of the lingual artery and coronary atherosclerosis. British Journal of Oral & Maxillofacial Surgery. 1995;33(5):309-11.

14. Gaibazzi N, Rigo F, Reverberi C. Severe Coronary Tortuosity or Myocardial Bridging in Patients With Chest Pain, Normal Coronary Arteries, and Reversible Myocardial Perfusion Defects. The American Journal of Cardiology. 2011;108(7):973-8.

15. Gallo D, Steinman DA, Morbiducci U. An Insight into the Mechanistic Role of the Common Carotid Artery on the Hemodynamics at the Carotid Bifurcation. Ann Biomed Eng. 2014.

16. Wood NB, Zhao SZ, Zambanini A, Jackson M, Gedroyc W, Thom SA, et al. Curvature and tortuosity of the superficial femoral artery: a possible risk factor for peripheral arterial disease. J Appl Physiol. 2006;101(5):1412-8.

17. Hart WE, Goldbaum M, Côté B, Kube P, Nelson MR. Measurement and classification of retinal vascular tortuosity. International journal of medical informatics. 1999;53(2-3):239-52.

18. Smedby Ö, Bergstrand L. Tortuosity and atherosclerosis in the femoral artery: What is cause and what is effect? Annals of Biomedical Engineering. 1996;24(4):474-80.

19. Piccinelli M, Veneziani A, Steinman DA, Remuzzi A, Antiga L. A Framework for Geometric Analysis of Vascular Structures: Application to Cerebral Aneurysms. IEEE Transactions on Medical Imaging. 2009;28; 31(8):1141-55.

20. O'Flynn PM, O'Sullivan G, Pandit AS. Methods for three-dimensional geometric characterization of the arterial vasculature. Ann Biomed Eng. 2007;35(8):1368-81.

21. Alastruey J, Siggers JH, Peiffer V, Doorly DJ, Sherwin SJ. Reducing the data: Analysis of the role of vascular geometry on blood flow patterns in curved vessels. Physics of Fluids. 2012;24(3):031902.

22. Alastruey J, Khir AW, Matthys KS, Segers P, Sherwin SJ, Verdonck PR, et al. Pulse wave propagation in a model human arterial network: Assessment of 1-D visco-elastic simulations against in vitro measurements. Journal of Biomechanics. 2011;44(12):2250-8.

23. Dean WR. Note on the motion of fluid in a curved pipe. London, Edinburgh, and Dublin Philosophical Magazine and Journal of Science. 1927;4(20):208-23.

24. Berger SA, Talbot L, Yao LS. Flow in Curved Pipes. Annual Review of Fluid Mechanics. 1983;15(1):461-512.

25. Li Y, Shi Z, Cai Y, Feng Y, Ma G, Shen C, et al. Impact of Coronary Tortuosity on Coronary Pressure: Numerical Simulation Study. PLoS ONE. 2012;7(8):e42558.

26. Kaplan AD, Jaffa AJ, Timor IE, Elad D. Hemodynamic Analysis of Arterial Blood Flow in the Coiled Umbilical Cord. Reproductive Sciences. 2010;17(3):258-68.

27. Xie X, Wang Y, Zhu H, Zhou H, Zhou J. Impact of Coronary Tortuosity on Coronary Blood Supply: A Patient-Specific Study. PLoS ONE. 2013;8(5):e64564.

28. Chien S. Effects of disturbed flow on endothelial cells. Ann Biomed Eng. 2008;36(4):554-62.

29. Li Y, Shen CX, Ji YN, Feng Y, Ma GS, Liu NF. Clinical Implication of Coronary Tortuosity in Patients with Coronary Artery Disease. PLoS ONE. 2011;6(8):e24232.

30. Xie X, Wang Y, Zhu H, Zhou J. Computation of hemodynamics in tortuous left coronary artery: a morphological parametric study. Journal of Biomechanical Engineering. 2014;136(10):101006.

31. Pedley TJ. The fluid mechanics of large blood vessels. Cambridge; New York: Cambridge University Press; 1980.

32. Siggers JH, Waters SL. Steady flows in pipes with finite curvature. Physics of Fluids. 2005;17(7):77102.

33. Van Canneyt K, Morbiducci U, Eloot S, De Santis G, Segers P, Verdonck P. A computational exploration of helical arterio-venous graft designs. Journal of Biomechanics. 2013;46(2):345-53.

34. Qiao AK, Guo XL, Wu SG, Zeng YJ, Xu XH. Numerical study of nonlinear pulsatile flow in S-shaped curved arteries. Medical engineering & physics. 2004;26(7):545-52.

35. Xie X, Wang Y, Zhou H. Impact of coronary tortuosity on the coronary blood flow: a 3D computational study. Journal of biomechanics. 2013;46(11):1833-41.

36. Caro CG, Cheshire NJ, Watkins N. Preliminary comparative study of small amplitude helical and conventional ePTFE arteriovenous shunts in pigs. Journal of The Royal Society Interface. 2005;2(3):261-6.

37. Yushkevich PA, Piven J, Hazlett HC, Smith RG, Ho S, Gee JC, et al. User-guided 3D active contour segmentation of anatomical structures: Significantly improved efficiency and reliability. NeuroImage. 2006;31(3):1116-28.

38. http://meshlab.sourceforge.net/.

39. Choi G, Cheng CP, Wilson NM, Taylor CA. Methods for quantifying three-dimensional deformation of arteries due to pulsatile and nonpulsatile forces: implications for the design of stents and stent grafts. Ann Biomed Eng. 2009;37(1):14-33.

40. Dougherty G, Johnson MJ. Clinical validation of three-dimensional tortuosity metrics based on the minimum curvature of approximating polynomial splines. Medical Engineering and Physics. 2008;30(2):190-8.

41. Sangalli LM, Secchi P, Vantini S, Veneziani A. A Case Study in Exploratory Functional Data Analysis: Geometrical Features of the Internal Carotid Artery. JOURNAL OF THE AMERICAN STATISTICAL ASSOCIATION. 2009;104(485):37-48.

42. Sangalli LM, Secchi P, Vantini S, Veneziani A. Efficient estimation of three-dimensional curves and their derivatives by free-knot regression splines, applied to the analysis of inner carotid artery centrelines. Journal of the Royal Statistical Society: Series C (Applied Statistics). 2009;58(3):285-306.

43. Davies JE, Parker KH, Mayet J, Whinnett ZI, Francis DP, Manisty CH, et al. Evidence of a dominant backward-propagating "suction" wave responsible for diastolic coronary filling in humans, attenuated in left ventricular hypertrophy. Circulation. 2006;113(14):1768-78.

44. van der Giessen AG, Groen HC, Doriot P-A, de Feyter PJ, van der Steen AFW, van de Vosse FN, et al. The influence of boundary conditions on wall shear stress distribution in patients specific coronary trees. Journal of Biomechanics. 2011;44(6):1089-95.

45. Pietrabissa R, Mantero S, Marotta T, Menicanti L. A lumped parameter model to evaluate the fluid dynamics of different coronary bypasses. Medical engineering & physics. 1996;18(6):477-84.

46. Seo T, Schachter LG, Barakat AI. Computational study of fluid mechanical disturbance induced by endovascular stents. Ann Biomed Eng. 2005;33(4):444-56.

47. Papanastasiou TC, Georgiou GC, Alexandrou AN. Viscous fluid flow. Boca Raton, Fla: CRC Press; 2000.

48. Lyne WH. Unsteady viscous flow in a curved pipe. Journal of Fluid Mechanics. 1971;45:13-31.

49. Germano M. On the effect of torsion on a helical pipe flow. Journal of Fluid Mechanics. 1982;125(1):1-8.

50. Gallo D, Steinman DA, Bijari PB, Morbiducci U. Helical flow in carotid bifurcation as surrogate marker of exposure to disturbed shear. Journal of biomechanics. 2012;45(14):2398-404.

51. Aristokleous N, Seimenis I, Georgiou GC, Papaharilaou Y, Brott BC, Nicolaides A, et al. Impact of Head Rotation on the Individualized Common Carotid Flow and Carotid Bifurcation Hemodynamics. IEEE Journal of Biomedical and Health Informatics. 2014;18(3):783-9.

52. Morbiducci U, Ponzini R, Gallo D, Bignardi C, Rizzo G. Inflow boundary conditions for image-based computational hemodynamics: impact of idealized versus measured velocity profiles in the human aorta. Journal of Biomechanics. 2013;46(1):102-9.

53. Chiastra C, Morlacchi S, Gallo D, Morbiducci U, Cárdenes R, Larrabide I, et al. Computational fluid dynamic simulations of image-based stented coronary bifurcation models. Journal of the Royal Society, Interface / the Royal Society. 2013;10(84):20130193.

54. Ku DN, Giddens DP, Zarins CK, Glagov S. Pulsatile flow and atherosclerosis in the human carotid bifurcation. Positive correlation between plaque location and low oscillating shear stress. Arteriosclerosis (Dallas, Tex). 1985;5(3):293.

55. Malek AM, Alper SL, Izumo S. Hemodynamic shear stress and its role in atherosclerosis. JAMA : the journal of the American Medical Association. 1999;282(21):2035-42.

56. Chatzizisis YS, Coskun AU, Jonas M, Edelman ER, Feldman CL, Stone PH. Role of endothelial shear stress in the natural history of coronary atherosclerosis and vascular remodeling - Molecular, cellular, and vascular behavior. Journal of the American College of Cardiology. 2007;49(25):2379-93.

57. Caro CG. Discovery of the role of wall shear in atherosclerosis. Arteriosclerosis, thrombosis, and vascular biology. 2009;29(2):158-61.

58. Himburg HA, Grzybowski DM, Hazel AL, LaMack JA, Li X-M, Friedman MH. Spatial comparison between wall shear stress measures and porcine arterial endothelial permeability. American Journal of Physiology - Heart and Circulatory Physiology. 2004;286(5):H1916-22.

59. Hoi Y, Zhou Y-Q, Zhang X, Henkelman RM, Steinman DA. Correlation between local hemodynamics and lesion distribution in a novel aortic regurgitation murine model of atherosclerosis. Ann Biomed Eng. 2011;39(5):1414-22.

60. Lee S-W, Antiga L, Spence JD, Steinman DA. Geometry of the carotid bifurcation predicts its exposure to disturbed flow. Stroke; a journal of cerebral circulation. 2008;39(8):2341-7.

61. Lee S-W, Antiga L, Steinman DA. Correlations among indicators of disturbed flow at the normal carotid bifurcation. Journal of Biomechanical Engineering. 2009;131(6):061013-7.

62. Dean WR. LXXII. The stream-line motion of fluid in a curved pipe (Second paper). Philosophical Magazine Series 7. 1928;5(30):673-95.

63. Prosi M, Perktold K, Ding Z, Friedman MH. Influence of curvature dynamics on pulsatile coronary artery flow in a realistic bifurcation model. Journal of Biomechanics. 2004;37(11):1767-75.

64. Malvè M, Gharib AM, Yazdani SK, Finet G, Martínez MA, Pettigrew R, et al. Tortuosity of Coronary Bifurcation as a Potential Local Risk Factor for Atherosclerosis: CFD Steady State Study Based on In Vivo Dynamic CT Measurements. Ann Biomed Eng. 2015;43(1):82-93.

3 Conclusion and future steps

The aim of this work was to investigate an influence of coronary tortuosity on flow alterations and concomitant health problems. The investigation consisted of two parts: an idealized and patient-specific study. The idealized study focused on an investigation of one of aspects of tortuosity - curvature in the absence of tortuosity due to a heart shape. The 3D simplified geometries of tortuous coronary arteries were built. The qualitative analysis of the 2D coronary angiograms was performed to define a number of curved bends and bend amplitudes. Three simplified vessels were built with the number of bends ranging from five to seven and decreasing amplitude of each consecutive bend. In the patient-specific study, realistic geometries of tortuous coronary arteries were built from the 3D computed tomography angiographies using a segmentation process. In the contrast to the idealized geometries, the patient-based geometries include all aspects of coronary tortuosity. Three patient-based cases resulted in 23 coronary vessels that were used to perform a statistical analysis of a correlation between coronary tortuosity and flow alterations inside coronary arteries. A segmentation process, mesh building, computational and post-processing methods were successfully validated and implemented on the simulated data set providing a good starting point for further investigations regarding the coronary tortuosity. For all vessel geometries, pressure drop per unit length, wall shear stress distribution, helicity intensity, and a degree of tortuosity using distance, total curvature, and total torsion metrics were calculated.

In both studies it was shown that coronary tortuosity may lead to perfusion defects under certain conditions, such as exercising, because the force required to drive the blood through a more tortuous vessel is higher than in a less tortuous one resulting in a higher pressure drop downstream the vessel. An investigation of idealized cases showed that higher tortuosity may increase a risk of atherosclerosis. At the same time, the patient-specific study indicated that tortuosity, in fact, suppresses the risk of atherosclerosis. That result signifies that tortuosity may be used to counterbalance the risk of atherosclerosis in coronary arteries that have other predispositions to atherosclerosis. The disagreement between the results of simplified and realistic cases indicates that different aspects of the tortuosity may have an opposite influence on the flow in coronary arteries: the curvature aspect of tortuosity leads to an increased risk of coronary artery disease, while the curvature coupled with torsion and tortuosity due to the heart

shape has atheroprotective influence on the hemodynamics. Thus, modeling of coronary tortuosity should take into account all aspects of tortuosity, like curvature and torsion, and consider the hearth shape as well.

Another important result that was obtained in this project is that the helicity intensity may be a good potential universal parameter to describe coronary tortuosity. It was shown that the helicity intensity depends on the degree of tortuosity and is sufficiently correlated with alterations of other flow parameters that can increase risks of unhealthy conditions in the heart. In further investigations, the helicity intensity should be tried as a parameter that will serve to define a severity of tortuosity of a coronary artery, as a tortuosity index, and be used as a predictor of flow alterations and accompanying affects on health conditions of a patient.

In future, to perform a stronger statistical analysis of coronary tortuosity, it is necessary to acquire more clinical data (computed tomography angiograms (CTAs)) showing tortuous coronary arteries without significant coronary artery disease. Increasing number of patient-specific cases will allow obtaining a relation of tortuosity metrics to the flow parameters with a better precision. Moreover, to reduce an uncertainty due to the segmentation process, higher resolution of the clinical data can be used.

It will also be interesting to improve the analysis discussed in Chapter 2 by subtracting tortuosity due to the heart shape from the metrics and investigating the correlation between new tortuosity metrics and flow parameters.

There is a considerable interest in developing an automated coronary angiogram or CTA processing method to classify patients by a degree of tortuosity and a tortuosity index based on numerical and clinical study that investigate an impact of tortuosity degree on different clinical conditions and flow alterations. A classification of geometry of coronary arteries by tortuosity degree is the first step toward identifying specific geometric features that increase patient susceptibility to myocardial perfusion defects.

Establishing an automated method to measure a coronary tortuosity degree from clinical data will also permit epidemiological studies of whether coronary tortuosity has a prognostic significance independent of other risk predictors like a coronary artery disease. Also, watching the tortuosity progression over time might allow a cardiologist to measure the effectiveness of certain therapies for blood pressure control or a regression of left ventricular hypertrophy.

Defining a tortuosity index, based on the tortuosity degree, will allow interventional cardiologists to standardize their approaches to interventions in these vessels.

Appendix A. Image segmentation and mesh

A.1. Image segmentation

The segmentation of the CTA coronary vessel was performed in the ITK-SNAP software (1). The three projections of the CTA are shown in Figure 11 (a-c). The segmentation in process is shown at the bottom left part of Figure 11 (d). First, the CTA image contrast and brightness are adjusted to make the coronary arteries more visible. Then, they are colored using automatic snake-roi tool, or manually, in all three projections building the segmentation.

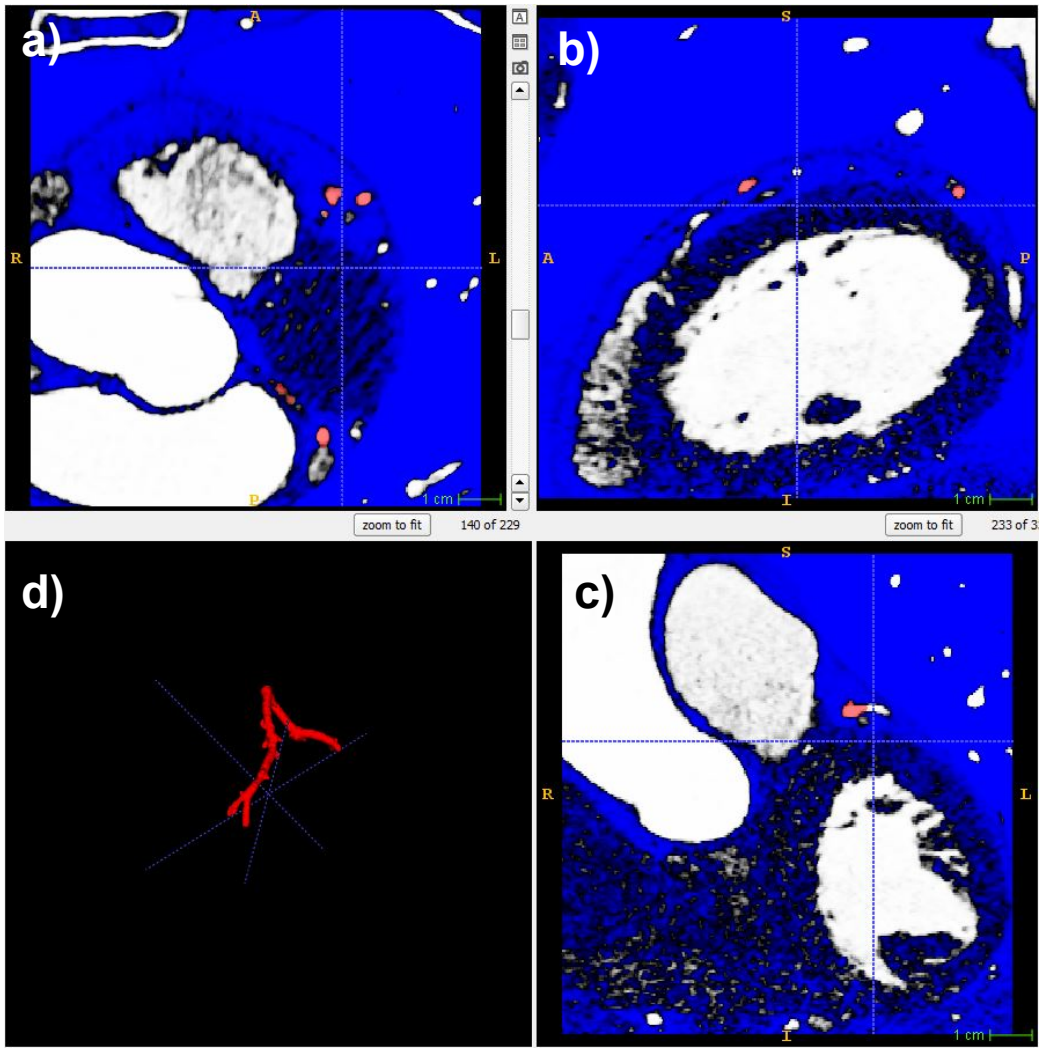

Figure 11. Segmentation of the vessels from computed tomography angiogram (CTA) for patient-A using ITK-SNAP: the vessels are colored in three different projections of the CTA (a-c), the segmentation object in process can be seen in (d).

The resulted segmentation was improved where the automatic or manual segmentation failed; it was smoothed using MeshLab (2) and Geomagic Studio® (3D Systems, Cary, NC, USA) (Figure 12). Next step was to extract a surface for the following use in the meshing tool. The surface was extracted by means of Geomagic Studio in which patch layout for the smoothed segmentation was built. Then a grid was constructed for each patch, and the reproducible surface was fitted to the constructed grid on the underlying polygon mesh (Exact Surface Phase or Parametric Surface Phase). That was performed to create a two-dimensional section of the Polygon object that can be reconstructed in an external CAD system.

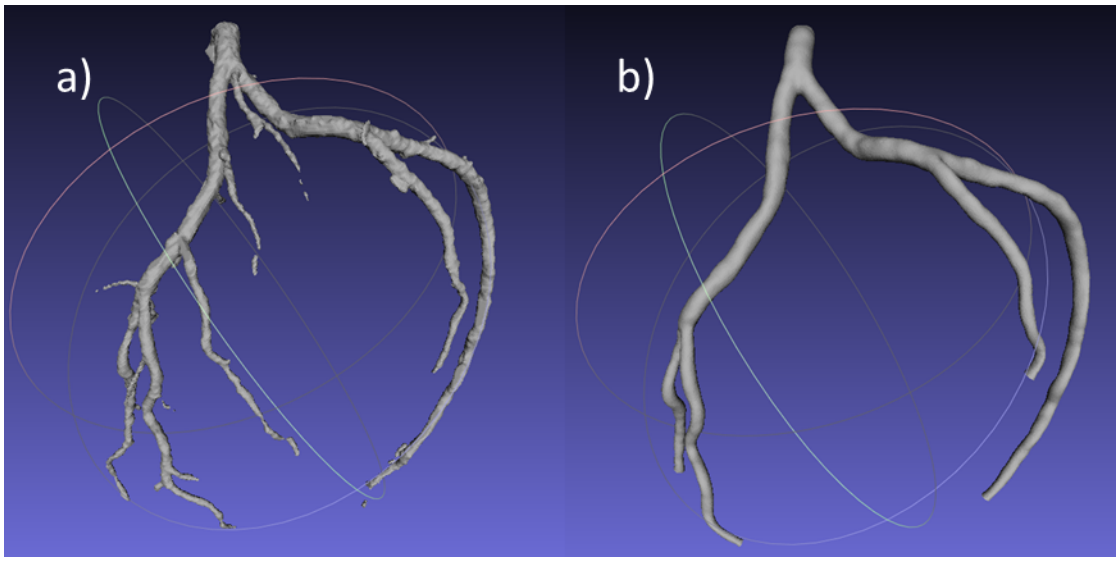

Figure 12. The segmentation polygon surface obtained in ITK-SNAP (a) and the cleaned and smoothed polygon mesh obtained in MeshLab (b)

A.2. Mesh

For both idealized and patient-specific studies, the o-grid type mesh was built. To build the o-grid type mesh, it is required to build the blocking first. The mesh was built in ANSYS ICEM-CFD. A mesh for the idealized study is shown in Figure 13, while the blocking and a mesh for patient-specific study are shown in Figure 14. For the idealized geometries, the same blocking type was used as for the patient-specific geometries. As one of the main quantities of interest is the wall shear stress, 10 prism layers were built near the wall to ensure the sufficient discretization of the mesh near the wall.

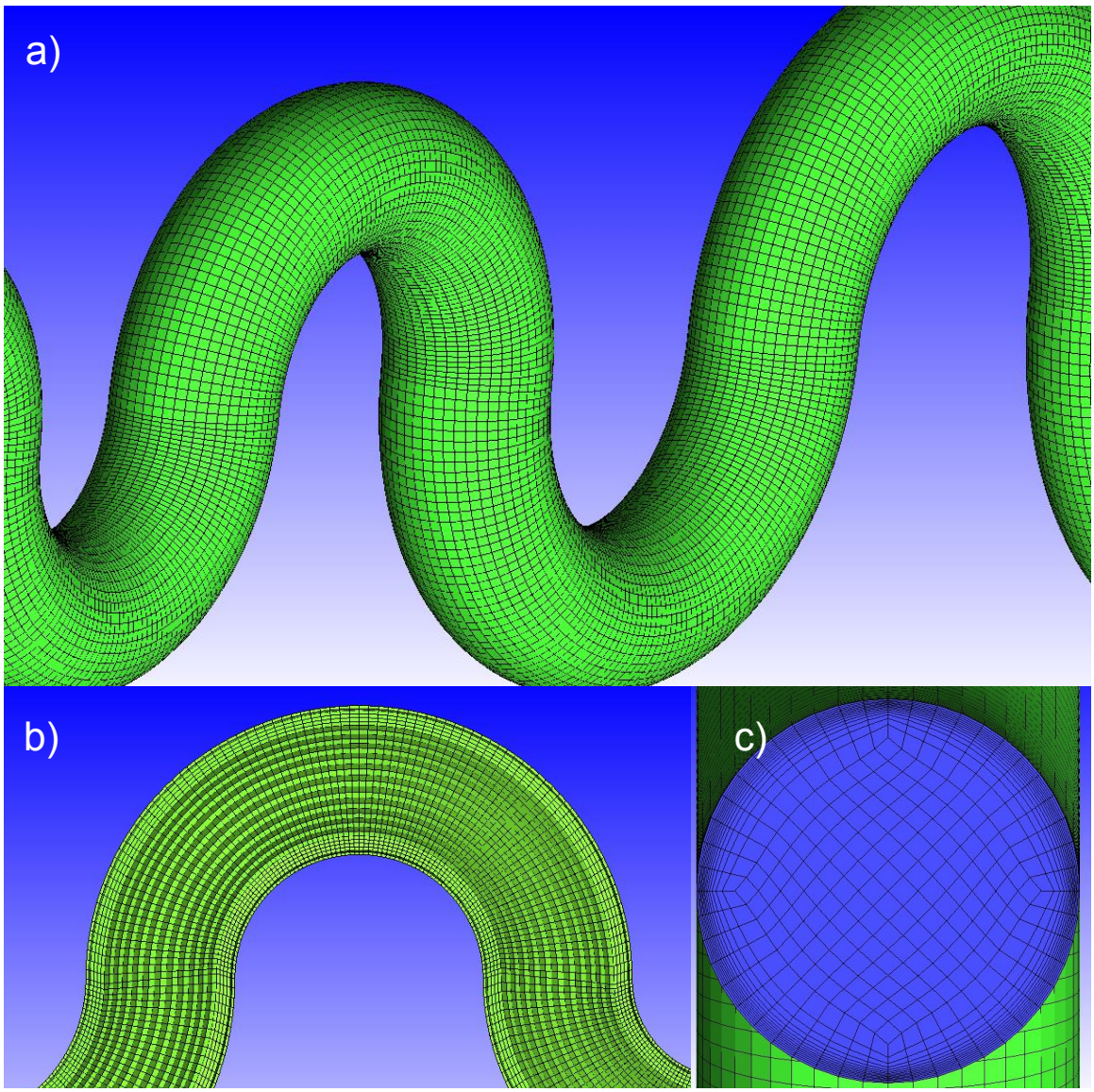

Figure 13. The O-grid mesh with 10 prism layers for idealized study, the case without branch: (a) the mesh view from the side, (b) the axial cross-section view, (c) transverse cross-section view.

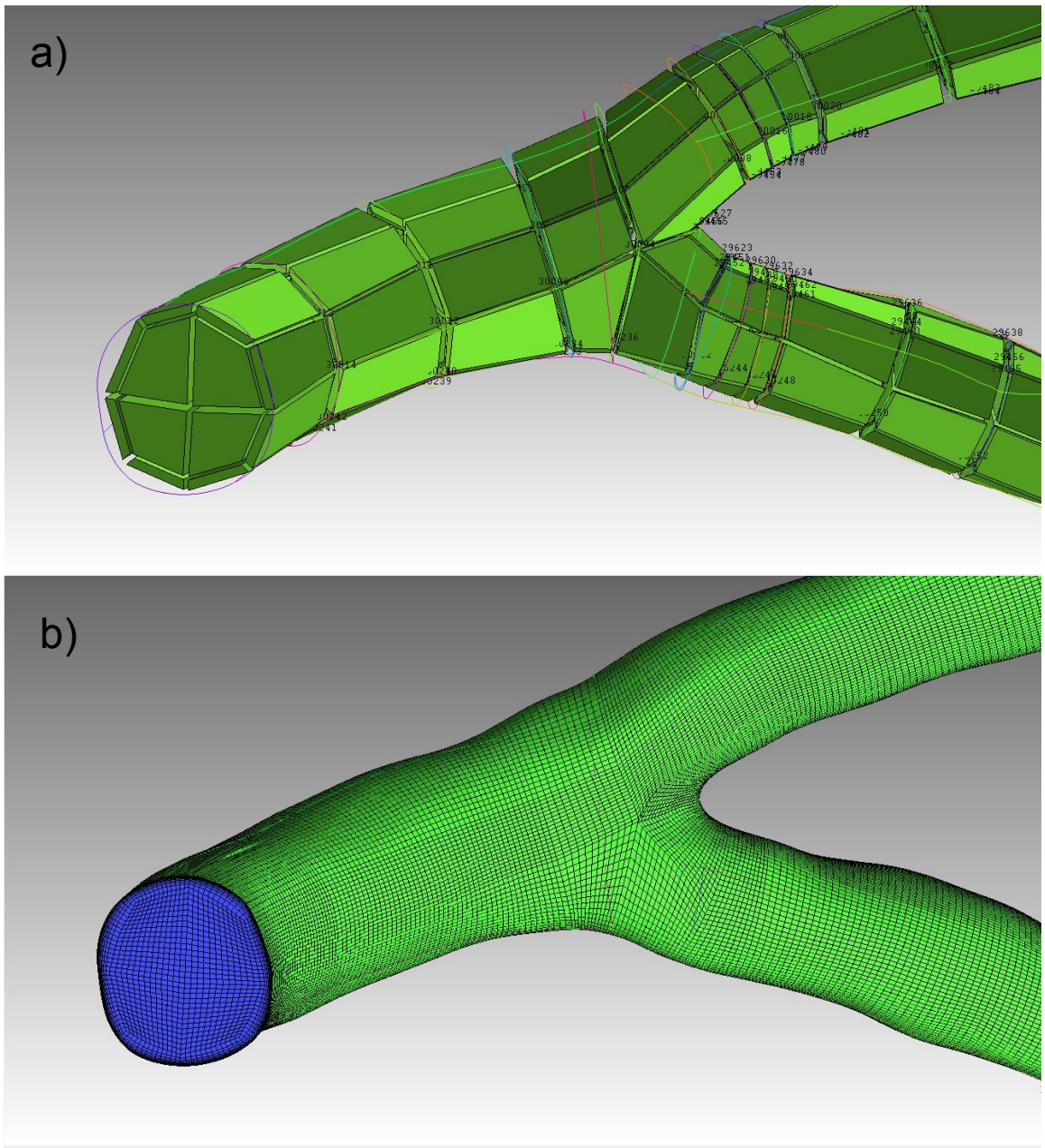

Figure 14. Blocking (a) and o-grid mesh (b) for patient-specific study case of patient-A.

References

1. Yushkevich PA, Piven J, Hazlett HC, Smith RG, Ho S, Gee JC, et al. User-guided 3D active contour segmentation of anatomical structures: Significantly improved efficiency and reliability. NeuroImage. 2006;31(3):1116-28.

2. http://meshlab.sourceforge.net/.

Appendix B. Fluid dynamics model details

B.1. Non-Newtonian model

Carreau model is used to model the non-Newtonian behavior of the blood:

$$\mu = \mu_\infty + \left(\mu_0 - \mu_\infty\right)\left[1 + \left(\lambda \dot{S}\right)^2\right]^{(n-1)/2}, \tag{12}$$

where μ is the dynamic viscosity, μ_0 and μ_∞ are the viscosity values as the shear rate goes to zero and infinity, $\dot{S}$ is the shear rate, λ is the time constant, and n is the power-law index. These parameters have the following values (1):

$$\mu_\infty = 0.0035\ Pa\ s,\ \mu_0 = 0.25\ Pa\ s,\ \lambda = 25\ s,\ n = 0.25\ .$$

B.2. Boundary conditions

B.2.1. Inlet boundary condition

At the inlet a uniform velocity profile was set with the axial velocity following shape of the representative velocity in LMCA for patient specific studies and in LAD for idealized cases (2). The Fourier fits were built for these representative velocities using 7 Fourier terms (Figure 15) for the calculations.

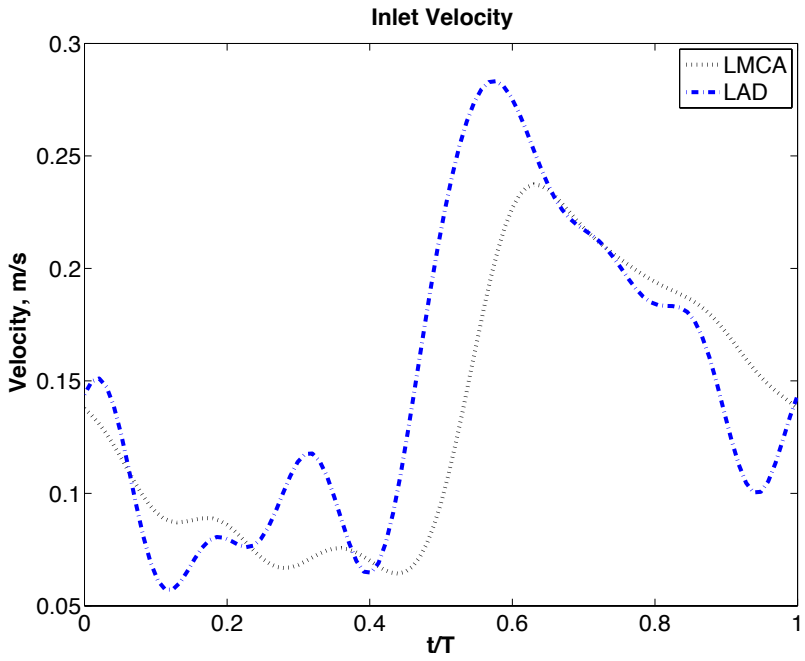

Figure 15. Velocity curves for the representative LAD and LMCA branches.

The number of the Fourier terms for the study was chosen so that the solution pressure and velocity curves do not have a high frequency noise.

The average flow rate was adjusted for each patient-specific case according to a law proposed by van Giessen *et al.* (3):

$$q = 1.43 d^{2.55} \ , \tag{13}$$

where q is the flow rate, and d is the diameter of the inlet.

B.2.2. Outlet boundary condition

The solution of the blood flow in coronary arteries is highly dependent on the outflow boundary conditions. For the studies where the pressure field distribution is not investigated and only the pressure gradients are investigated, the simplest way to set up boundary conditions for transient coronary flow calculations with one outlet is to prescribe a realistic velocity profile at the inlet and constant pressure at the outlet. For the idealized cases, we use the constant pressure boundary condition.

The constant boundary condition was shown to give unrealistic results for multiple outlets models (4, 5), and for the cases with several outlets the radius-dependent flow split boundary condition can be applied (5). The flow split at the bifurcation of the vessel into two daughter branches was derived using the same measurements that were used to derive equation (1) and is calculated as follows (3):

$$\frac{q_{D_2}}{q_{D_1}} = \left(\frac{d_{D_1}}{d_{D_2}} \right)^{2.27} . \tag{14}$$

As numerical models get more advanced, more realistic boundary conditions are introduced to consider the influence of the downstream or upstream vasculatures on the computational domain. Using simple models the downstream vasculatures can be taken into account by such boundary conditions as the resistance model, Windkessel model or other lumped parameter models which couple flow rate and pressure in the numerical domain to a reduced-order model or "lumped parameter" model (4-7). A general difficulty for setting up these types of boundary conditions is to define the parameter(s) required for each outlet to set them up.

The outlet boundary condition for patient-specific cases in the project is modeled by the most simple lumped parameter model, the resistance boundary condition, with the outlet pressure calculated at each time step as:

$$p(t) = R \cdot q(t) , \tag{15}$$

where R is the resistance of the entire downstream vascular system, and q is the flow rate at the outlet. The resistance values were taken from Pietrabissa *et al.* (8). In this study, the resistance values downstream each branch outlet were estimated from experimental pressure/flow measurements of capillary bed resistance values.

There are many more different models to set up the BCs such as Windkessel model (9), Structured-Tree model (10), which go out of bounds of the current study.

References

1. Seo T, Schachter LG, Barakat AI. Computational study of fluid mechanical disturbance induced by endovascular stents. Ann Biomed Eng. 2005;33(4):444-56.

2. Davies JE, Parker KH, Mayet J, Whinnett ZI, Francis DP, Manisty CH, et al. Evidence of a dominant backward-propagating "suction" wave responsible for diastolic coronary filling in humans, attenuated in left ventricular hypertrophy. Circulation. 2006;113(14):1768-78.

3. van der Giessen AG, Groen HC, Doriot P-A, de Feyter PJ, van der Steen AFW, van de Vosse FN, et al. The influence of boundary conditions on wall shear stress distribution in patients specific coronary trees. Journal of Biomechanics. 2011;44(6):1089-95.

4. Vignon-Clementel IE, Alberto Figueroa C, Jansen KE, Taylor CA. Outflow boundary conditions for three-dimensional finite element modeling of blood flow and pressure in arteries. Computer Methods in Applied Mechanics and Engineering. 2006;195(29–32):3776-96.

5. Sommer K, Schmidt R, Graafen D, Breit HC, Schreiber LM. Contrast agent bolus dispersion in a realistic coronary artery geometry: influence of outlet boundary conditions. Ann Biomed Eng. 2014;42(4):787-96.

6. Williams AR, Koo B-K, Gundert TJ, Fitzgerald PJ, LaDisa JJF. Local hemodynamic changes caused by main branch stent implantation and subsequent virtual side branch balloon angioplasty in a representative coronary bifurcation. Journal of applied physiology (Bethesda, Md : 1985). 2010;109(2):532-40.

7. Taylor CA, Figueroa CA. Patient-Specific Modeling of Cardiovascular Mechanics. Annual Review of Biomedical Engineering. 2009;11:109-34.

8. Pietrabissa R, Mantero S, Marotta T, Menicanti L. A lumped parameter model to evaluate the fluid dynamics of different coronary bypasses. Medical engineering & physics. 1996;18(6):477-84.

9. Westerhof N, Lankhaar JW, Westerhof BE. The arterial Windkessel. Med Biol Eng Comput. 2009;47(2):131-41.

10. Olufsen MS, Peskin CS, Kim WY, Pedersen EM, Nadim A, Larsen J. Numerical simulation and experimental validation of blood flow in arteries with structured-tree outflow conditions. Annals of Biomedical Engineering. 2000;28(11):1281-99.

Appendix C. Estimation of numerical errors in the simulation

This section is written based on the Oberkampf and Roy's book "Verification and Validation in scientific computing" (1). Quantifying the numerical errors is important for establishing numerical accuracy of a simulation for model validation purposes.

C.1. Rounding off error

For the solution quantities of interest, the relative rounding off errors estimate can be calculated as follows:

$$\epsilon_{ro} = \frac{\left| f_{\sin gle} - f_{double} \right|}{f_{double}} \times 100\%, \tag{16}$$

where f_{single} is the solution calculated with single precision and f_{double} is the solution calculated with double precision. In the project the calculations are done with double precision.

C.2. Iterative error

An iterative error is the difference between the current approximate solution to a system of equations and the exact solution. While monitoring of the iterative residuals often serves as an adequate indication to whether iterative convergence has been achieved, it does not by itself provide any guidance as to the amount of the iterative error in the solution quantities of interest. In this study we use the machine zero method to estimate relative iterative convergence:

$$\left| \frac{f_{i\to\infty} - f_{i^{th}iteration}}{f_{i\to\infty}} \right| \times 100\%, \tag{17}$$

where $f_{i\to\infty}$ is the machine zero solution, i.e. the iterative solution found in the limit as the number of iterations goes to infinity. This location can be identified as the point in the iteration history where the residuals no longer reduce, but instead display seemingly random oscillations about some value.

C.3. Relative discretization error

Discretization errors are those associated with the mesh resolution and quality, as well as the time step chosen for unsteady problem. Discretization error is formally defined as the difference between the exact solution to the discrete equations and the exact solution to the mathematical model. To estimate the relative discretization method, we are using the mesh refinement method based on a general concept of Richardson extrapolation (2). The power series expansion can be used to relate the discretization error in a solution quantity of interest $\epsilon_h = f_h - \tilde{f}$ to mesh spacing parameter h, which for a convergent, 2nd-order discretization, can be written as

$$f_h - \tilde{f} = g_2 h^2 + O(h^3) \ , \tag{18}$$

where f_h is the discrete solution, and $\tilde{f}$ is the exact solution to the mathematical model. Then, two discrete solutions on systematically refined[3] meshes are computed. Using formula (3) the estimate of the exact solution to the mathematical model can be calculated as follows:

$$\tilde{f} = f_h + \frac{f_h - f_{rh}}{r^2 - 1} \ , \tag{19}$$

where r is the refinement ratio.

This estimate will only be reliable in the asymptotic range where the terms of order h^3 and higher can be neglected. In the asymptotic range, the estimate is generally accurate to within third order. The formulas (6) and (7) can be generalized for the p^{th}-order discretization scheme.

C.4. Observed order of accuracy

To assess the confidence in the discretization error estimate, the observed order of accuracy can be calculated. When the observed order of accuracy is shown to match the formal order, one can have a high degree of confidence that the error estimate is reliable.

---

[3] Systematic mesh refinement requires that the mesh is refined by the same factor over the entire domain and the consistency of the refinement as h->0. Consistent refinement requires that the mesh quality must either remain constant or improve with mesh refinement

Consider pth order of accurate scheme with numerical solutions on a fine mesh (h_1), a medium mesh (h_2), and a course mesh (h_3). For the case of the constant grid refinement $r = \frac{h_2}{h_1} = \frac{h_3}{h_2} > 1$, the observed order of accuracy can be calculated as follows:

$$\hat{p} = \frac{\ln\left(\frac{f_3 - f_2}{f_2 - f_1}\right)}{\ln(r)} \ . \tag{20}$$

The formula is derived using the general discretization error expansion for the 2nd-order scheme shown in formula (6).

For the non-constant grid refinement, i.e. $r_{12} = \frac{h_2}{h_1} > 1, r_{23} = \frac{h_3}{h_2} > 1$, the apparent order of accuracy can be calculated by solving the following equation iteratively (3):

$$\frac{f_3 - f_2}{r_{23}^{\hat{p}} - 1} = r_{12}^{\hat{p}}\left(\frac{f_2 - f_1}{r_{12}^{\hat{p}} - 1}\right) . \tag{21}$$

C.5. Patient-specific study

C.5.1. Rounding off error

In this study, the relative rounding off error was calculated for the steady flow in the idealized geometry with 5 curved bends for the pressure drop. It is equal to $2.57\text{E-}07\%$. We suppose that for the rest of the idealized, patient-specific cases, and the rest of the system response quantities it will be comparably small and we neglect it in the estimation of the numerical uncertainty.

C.5.2. Iterative error

The relative iterative error is calculated for the values of area-weighted average pressure on the arbitrarily chosen cross-section ($AWAP_1$) of the LAD branch of the patient-A and area-weighted average of the wall shear stress (AWAWSS) on the vessel tree wall of the patient-A.

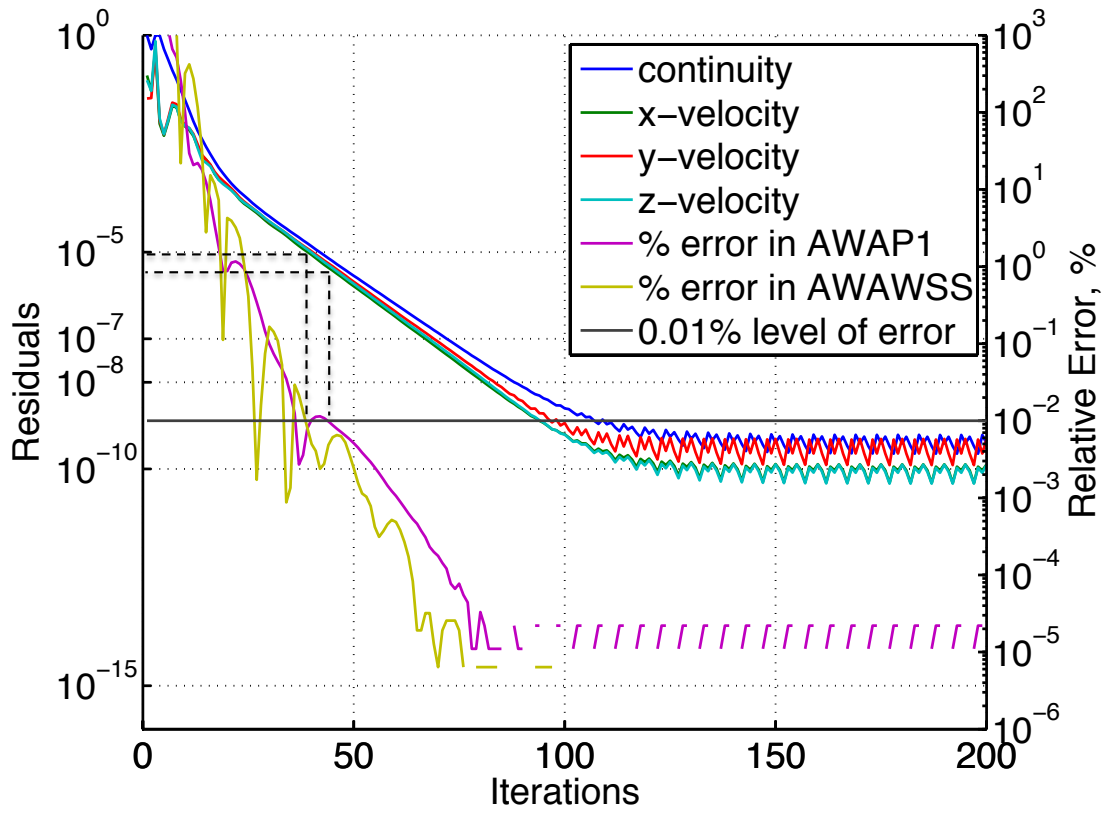

Figure 16. The residual history and the relative error history for the patient-A case with mesh size 0.2 mm for steady calculations. The relative error is calculated for area-weighted pressure at the plane-7 and for area-weighted average of the wall shear stress (AWAWSS).

For the patient-specific study, the iterative error for $AWAP_1$ and AWAWSS was estimated for the patient-A case for unsteady flow. Figure 16 shows the normalized residual history and the relative error history with indicated level of the 0.01% relative error. The residuals are normalized by the maximum residual value after 5 iterations. To achieve the 0.01% level of error, the convergence criterion for the normalized residuals should be set to about 10^{-5} - 10^{-6} for the patient-A case. For all the patient-specific calculations, we set the convergence criterion to 10^{-7} to ensure that the relative error (or relative iterative error) is less than 0.01%.

C.5.3. Relative Discretization Error

The coupled grid and time sensitivity analysis for the solution of patient-A was done. The relative discretization error and apparent order of accuracy for maximum value of $AWAP_1$ and maximum value AWAWSS during the cardiac cycle is shown in Table 1.

Table 3. The coupled grid and time sensitivity analysis for patient-A. Grid and time discretization information is given: refinement ratio r, mesh size in mm, number of time steps per cardiac cycle. The values of the area-weighted average of the pressure on the cross-section (AWAP1) of the LAD branch of the patient-A case and the area-weighted average of the wall shear stress (AWAWSS) for the whole wall of the patient-A case are given in the table.

r	mesh size, mm	# of time steps	$AWAP_1$, mm Hg	AWAWSS, Pa	$\hat{p}$ $AWAP_1$	$\hat{p}$ AWAWSS	RDE $AWAP_1$, %	RDE AWAWSS, %
1.35	0.2	800	2.43268	1.88255	6.81221	3.33028	0.0763	0.0027
1.36	0.27	600	2.43421	1.87811			0.5956	0.0068
	0.36	440	2.42167	1.86538				

We observe that RDE for both system response quantities, $AWAP_1$ and AWAWSS, does not exceed 0.1%.

References

1. Oberkampf WLRCJ. Verification and validation in scientific computing. New York: Cambridge University Press; 2010.

2. Richardson LF. The Approximate Arithmetical Solution by Finite Differences of Physical Problems Involving Differential Equations, with an Application to the Stresses in a Masonry Dam. Philosophical Transactions of the Royal Society of LondonSeries A, Containing Papers of a Mathematical or Physical Character. 1911;210:307-57.

3. Celik I, Karatekin O. Numerical Experiments on Application of Richardson Extrapolation With Nonuniform Grids. Journal of Fluids Engineering. 1997;119(3):584-90.

Appendix D. Flow parameters versus tortuosity metrics

In Figure 17, the scatterplots of flow parameters, pressure drop per unit length, TAWSS90 and RRT90, calculated for each of 23 vessel segments versus the corresponding tortuosity metrics DM, TT, and TC are shown. Figure 17 demonstrates the best fit of four simple regression fits: linear, logarithmic in tortuosity metrics, logarithmic in flow parameters, and logarithmic in both, flow parameters and tortuosity metrics.

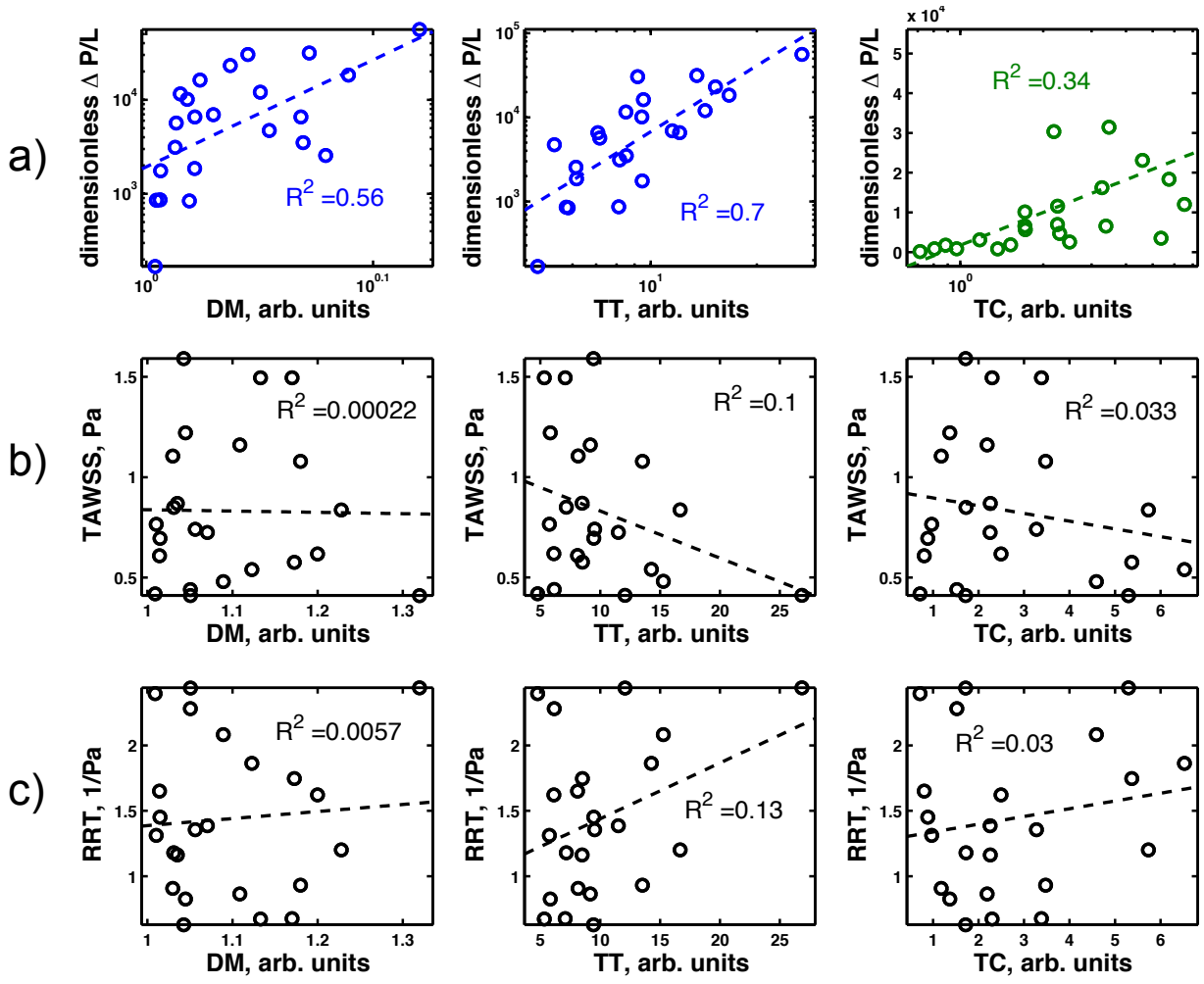

Figure 17. Scatterplots of the flow parameters: pressure drop per unit length (a), TAWSS90 (b) and RRT90 (c), calculated for each of 23 vessel segments against corresponding tortuosity metrics DM, TT, and TC. The color means different types of regression fits: blue – loglog fit, green – logx fit, black -linear fit.

We can see that there is no significant statistical correlation between WSS derived descriptors, TAWSS90 and RRT90, and tortuosity metrics, DM, TT and TC. There is a better correlation between pressure drop per unit length and DM and TT, but the correlation with TC is weak.

Appendix E. Helicity descriptors

In this work we studied an influence of helicity-based descriptors characterizing the bulk flow on hemodynamics parameters TAWSS90 and RRT90 described in Chapter 2. The first helicity descriptor is the intensity of the helical flow that can be calculated by an integration of the absolute value of H_k over the volume Ω of the vessel segment in study, and averaging over the cardiac cycle T (1, 2):

$$h_2 = \frac{1}{T\Omega}\int_0^T\int_\Omega |H_k| \, d\Omega \, dt \ . \tag{22}$$

A relation of helicity descriptor h_2 to hemodynamics parameters was investigated in detail in the manuscript Chapter 2. Here, we would like to introduce another helicity descriptor h_4 which was previously shown to be positively correlated with area of disturbed wall shear stress for carotid bifurcations (1). This descriptor is defined as follows:

$$h_4 = \frac{h_2}{\left| \frac{1}{T\Omega}\int_0^T\int_\Omega H_k \, d\Omega \, dt \right|} \ . \tag{1.23}$$

h_4 equals 0 in the presence of reflectional symmetry, and +1 when only right handed or only left handed structures are present.

In the following, we plot the values of h_4 for each of 23 vessel segments versus tortuosity metrics DM, TT, and TC. Figure 18 shows the best fit of four simple regression fits: linear logarithmic in tortuosity metrics, logarithmic in h_4, and logarithmic in both, h_4 and tortuosity metrics.

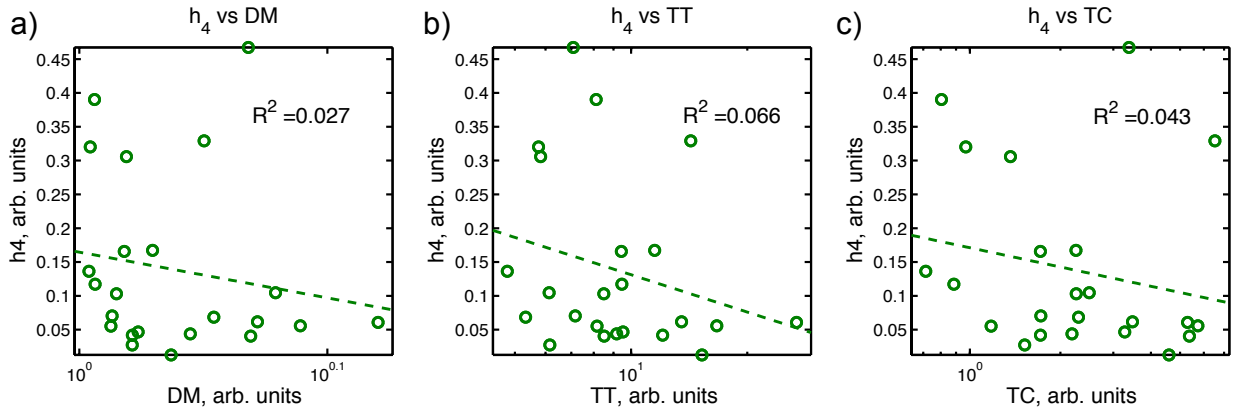

Figure 18. Scatter plots of the helicity descriptor h4 calculated for each of 23 vessel segments against tortuosity metrics: Distance Metric (DM) (a), Total Torsion metric (TT) (b), and Total Curvature metric (TC) (c). The dotted line shows the xlog regression fit to the data points. R2 is the determination coefficient.

We can see that there is no strong linear or logarithmic dependence between h_4 and tortuosity metrics (Figure 18), as well as there is no strong correlation between h_4 and hemodynamics parameters (Figure 19).

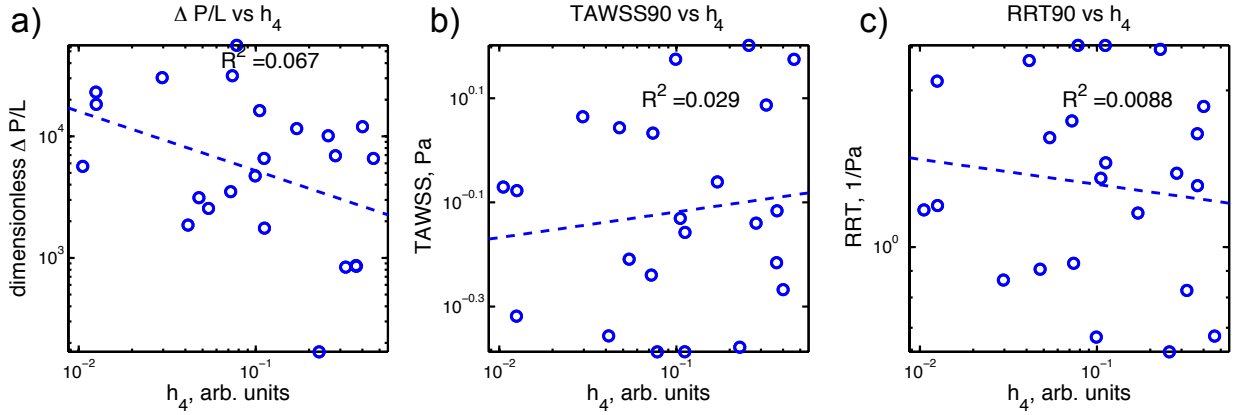

Figure 19. Scatter plots of the flow parameters: pressure drop per unit length, TAWSS90 and RRT90, calculated for each of 23 vessel segments plotted against corresponding helicity descriptor h_4. The dotted line shows the loglog regression fit to the data points. R2 is the determination coefficient.

References

1. Gallo D, Steinman DA, Bijari PB, Morbiducci U. Helical flow in carotid bifurcation as surrogate marker of exposure to disturbed shear. Journal of biomechanics. 2012;45(14):2398-404.

2. Gallo D, Steinman DA, Morbiducci U. An Insight into the Mechanistic Role of the Common Carotid Artery on the Hemodynamics at the Carotid Bifurcation. Ann Biomed Eng. 2014.

Appendix F. IRB approvals

CARILION CLINIC

March 6, 2013

David Sane, MD
Carilion Clinic Cardiology
127 McClanahan St., Suite 300

RE: Modeling of Arterial Tortuosity

Dear Dr. Sane:

This letter is to inform you that the application for your proposed study, received February 7, 2013, has been reviewed by the staff of the Carilion Institutional Review Board (IRB.)

The IRB has determined that your project does not require further IRB review because it does not meet the definition of human subjects research according to CFR §46.102(f.) Human subjects are defined as living individuals about whom an investigator conducting research obtains either data through intervention or interaction with the individual, or identifiable private information. Based on our review, we have concluded that the data involved in your study does not include identifiable private information and does not meet the above definition of human subjects. Therefore, IRB approval of this study is not necessary; however, separate arrangements must be made with the appropriate hospital or medical staff, departments or committees.

If any changes are made to your research that could affect our determination or classification of your project, you must notify the IRB. The IRB will then make a determination whether or not the research should remain in a non-human subjects research status.

We appreciate the opportunity to review your proposed study. We wish you every success.

Sincerely,

Charles A. Hite, MA, CIP, IRB Human Protections Administrator

cc: Daniel Harrington, MD, VP, Academic Affairs
Charles Schleupner, MD, Chair, Carilion IRB
Jeannie Perkins, Office of Sponsored Projects
Ralph Whatley, Chair, Medicine
IRB files

Institutional Review Board
2001 Crystal Spring Avenue, SW, Suite 202 Roanoke, VA 24014-2465 P.O. Box 13367 Roanoke, VA 24033-3367
540-853-0728 p 540-985-5323 f

CARILION CLINIC

February 17, 2014

David Sane, MD
Carilion Cardiology
127 McClanahan Street, Suite 300

Approval Date: February 17, 2014
Continuing Review Due Date: February 16, 2015
Expiration Date: February 16, 2015

re: Coronary Artery Tortuosity

Dear Dr. Sane:

I am pleased to inform you that the Carilion Institutional Review Board (IRB) has reviewed the above-mentioned protocol in an expedited manner according to 45 CFR 46.110 and 21 CFR 56.110. The research project was determined to present no more than minimal risk to human subjects and was found to have appropriate protections so that risks related to breach of confidentiality are no more than minimal. This research project met the expedited criteria outlined in 63 FR 60364-60367 category **(5)** Research involving materials (data, documents, records, or specimens) that have been collected, or will be collected solely for non-research purposes (such as medical treatment or diagnosis).

According to 45 CFR 46.111, the following requirements were satisfied in order for approval to be granted:

- risks were minimized;
- risks to subjects are reasonable in relation to anticipated benefits, if any, to the subjects, and to the importance of the knowledge that may reasonably result from the study;
- selection of the subjects was equitable given the purpose of the research;
- informed consent will be sought from and documented for each prospective subject unless the conditions for a waiver of documentation for consent were met;
- when appropriate, the research plan makes adequate provisions for monitoring the data collected to ensure safety of subjects; and
- adequate provisions to protect the privacy of the subjects and to maintain the confidentiality of the data were made.

The following research team members have received IRB approval to participate in the above-mentioned study: David Sane, Mathew Kalapurakal and Rodney Savage.

The following documents are IRB-approved: Protocol (IRB Application received 2/17/14) and Data Collection Tool (received 2/17/14.)

We have waived the requirement of informed consent as outlined in 45 CFR 46.116 (d). To meet the provisions of the waiver, the IRB has determined the research involves no more than minimal risk to the subjects; the waiver or alteration will not adversely affect the rights and welfare of the subjects; the research could not practicably be carried out without the waiver or alteration; and whenever appropriate, the subjects will be provided with additional pertinent information after participation.

Institutional Review Board
2001 Crystal Spring Avenue, SW, Suite 202 Roanoke, VA 24014-2465 PO Box 13367 Roanoke, VA 24033-3367
Phone: 540 853-0728 **Fax:** 540 985-5373

The Carilion IRB would like to thank you for allowing us the opportunity to review this protocol. We look forward to learning of your results.

Sincerely,

Charles A. Hite, MA, CIP
Human Protections Administrator

cc: Daniel Harrington, MD, VP, Academic Affairs
Charles Schleupner, MD, Chair, Carilion IRB
Jeannie Perkins, Administrative Director, Office of Sponsored Projects
Judie Snipes, Privacy Officer
Anne Marie Swindler, VP, Risk Management
Angela Steele, HIM
Mattie Tenzer, Director, Clinical Integration and Analytics
Ralph Whatley, MD, Chair, Dept. of Medicine
IRB files